(Un)Coupled thrust belt-foreland deformation in the northern Patagonian Andes: New insights from the Esquel-Gastre sector (41°30'-43°S)

E. Savignano, S. Mazzoli, M. Arce, M. Franchini, C. Gautheron, M. Paolini, M. Zattin

AGU PUBLICATIONS

Tectonics

RESEARCH ARTICLE
10.1002/2016TC004225

Key Points:
- New apatite (U-Th)/He ages were obtained for the Patagonian Andes at latitudes 41°30′-43°S
- The "broken foreland" area was characterized by Late Cretaceous to Paleogene exhumation
- Thrust belt-foreland (un)coupling of the deformation depends on steep- versus flat-slab subduction

Correspondence to:
E. Savignano,
elisa.savignano@studenti.unipd.it

Citation:
Savignano, E., S. Mazzoli, M. Arce, M. Franchini, C. Gautheron, M. Paolini, and M. Zattin (2016), (Un)Coupled thrust belt-foreland deformation in the northern Patagonian Andes: New insights from the Esquel-Gastre sector (41°30′–43°S), *Tectonics*, *35*, 2636–2656, doi:10.1002/2016TC004225.

Received 5 MAY 2016
Accepted 27 OCT 2016
Accepted article online 28 OCT 2016
Published online 19 NOV 2016

(Un)Coupled thrust belt-foreland deformation in the northern Patagonian Andes: New insights from the Esquel-Gastre sector (41°30′–43°S)

E. Savignano[1], S. Mazzoli[2], M. Arce[3], M. Franchini[3,4], C. Gautheron[5], M. Paolini[6], and M. Zattin[1]

[1]Department of Geosciences, University of Padua, Padova, Italy, [2]Department of Earth Sciences, University of Naples Federico II, Napoli, Italy, [3]Instituto de Investigación en Paleobiología y Geología, Universidad Nacional de Río Negro, Rio Negro, Argentina, [4]Centro Patagónico de Estudios Metalogenéticos, Universidad Nacional del Comahue, Neuquén, Argentina, [5]GEOPS, Univ Paris Sud, CNRS, Université Paris-Saclay, Orsay, France, [6]Ciudad Autónoma de Buenos Aires, Pan American Silver, Santa Cruz, Argentina

Abstract The Patagonian Andes represents a unique natural laboratory to study surface deformation in relation to deep slab dynamics. In the sector comprised between latitudes 41°30′ and 43°S, new apatite (U-Th)/He ages indicate a markedly different unroofing pattern between the "broken foreland" area (characterized by Late Cretaceous to Paleogene exhumation) and the adjacent Andean sector to the west, which is dominated by Miocene-Pliocene exhumation. These unroofing stages can be confidently ascribed to inversion tectonics involving reverse fault-related uplift and concomitant erosion. Late Cretaceous-Paleogene shortening and exhumation are well known to have affected also the thrust belt sector of the study area during a prolonged stage of flat-slab subduction. Therefore, the different ages of near-surface unroofing documented in this study suggest coupling of the deformation between the thrust belt and its foreland during periods of flat-slab subduction (e.g., during Late Cretaceous-Paleogene times) and dominant uncoupling during periods of steep-slab subduction and rollback, even when these are associated with high convergence rates (i.e., $>$ 4 cm/yr), as those documented in Miocene times for the Patagonian Andes.

1. Introduction

The process of far-field stress propagation from the orogen to the foreland plate is well known to occur and has been invoked to explain distributed weak strain recorded in large foreland sectors ahead of the thrust front [e.g., *Geiser and Engelder*, 1983]. However, modes of deformation in the foreland domain are dominantly of localized rather than distributed type. This is interpreted to be due to the fact that the continental lithosphere of the foreland plate is generally cooler and stronger with respect to that of the orogen, which is characterized by a warmer lithosphere and therefore a weaker rheology [*Butler and Mazzoli*, 2006]. In the Andes, basement shortening associated with strong inversion and uplift of the axial zone of the Permo-Triassic rift in the Eastern Cordillera of Peru, although being accommodated by localized shear involving widespread reactivation (at lower greenschist facies conditions) of inherited mesoscopic fractures, has been documented to represent a process of distributed strain at the orogen scale [*Mazzoli et al*., 2009]. This process has been invoked to explain internal straining of basement blocks in order to accommodate thick-skinned Andean shortening (e.g., in the Malargüe fold and thrust belt of Argentina, at latitudes 34–36°S) [*Mescua et al*., 2012]. Similarly, in the external Western Alps, the Variscan basement has been documented by *Bellahsen et al*. [2012] to have accommodated Alpine shortening by distributed slip along greenschist facies shear zones. According to these authors, although no significant reactivation of the inherited Jurassic normal faults took place there, the inherited synrift basins localized thick-skinned shortening due to the weakening associated with both the presence of less competent basin fills (that were disharmonically folded) and the *P-T* conditions experienced during crustal shortening. On the other hand, in the foreland lithosphere, localized deformation at the kilometer scale may be accommodated by inherited brittle structures that represent preferential zones of weakness [*Holdsworth et al*., 2001]. In this instance, positive inversion tectonics involving major reverse fault reactivation of deep-rooted discrete structures, particularly rift-related normal faults, is favored [*Ziegler*, 1987; *Coward*, 1994; *Ziegler et al*., 1995; *Lacombe and Mouthereau*, 2002; *Butler and Mazzoli*, 2006] and has been widely documented for the so-called "broken foreland" of the northern Patagonian Andes [*Humphreys*, 2009; *Ramos and Folguera*, 2009; *Folguera and Ramos*, 2011; *Orts et al*., 2012, 2015; *Gianni et al*., 2015a].

Classically, shortening is assumed to migrate ahead of the thrust front, progressively involving foreland domains that previously experienced flexure-related stretching [e.g., *Tavani et al*., 2015]. However, the situation is much more complex for the northern Patagonian fold and thrust belt and its foreland analyzed in this study (Figure 1a). Being located in the overriding plate of the Andean subduction system, this whole retroarc sector is interpreted to have experienced alternating shortening and upper plate extension during stages of flat- and steep-slab subduction, respectively [*Ramos and Folguera*, 2009; *Folguera and Ramos*, 2011; *Orts et al*., 2012, 2015]. More in general, several orogenic cycles of mountain building and subsequent extensional dismembering associated with periods of shallowing and steepening of the subducting plate have been recognized in recent years in the Andes [*Kley et al*., 1999; *Haschke et al*., 2002; *Kay and Coira*, 2009; *Ramos et al*., 2014]. These processes have been especially well documented for the southern Central Andes of Argentina and Chile between 34° and 37°S, where a complete cycle from crustal thickening and mountain building to extensional collapse has been unraveled and related to changes in the subduction geometry [*Ramos et al*., 2014]. On the other hand, the tectonic evolution of the Patagonian Andes further south is much less well known. Although a recent paper by *Echaurren et al*. [2016] provided important constraints based on the analysis of syntectonic strata, the degree of coupling versus uncoupling of the deformation between the thrust belt and its foreland during alternating stages of shallow underthrusting (i.e., flat-slab subduction) and of foundering of the subducting plate (i.e., slab rollback) needs to be further investigated. As a matter of fact, shortening and extension in the retroarc sector may vary not only in time (i.e., with major "cycles" of mountain building and orogenic collapse, respectively) but also in space, due to the variable transmission of horizontal compressive stress away from the orogen. Low-temperature (low-T) thermochronological systems are ideally suited for reconstructing thermal histories of rocks in the uppermost part of the crust because they record time and rates of cooling related to exhumation of the first kilometers of the crust. Presently, a rather extensive apatite fission track and apatite (U-Th)/He (AHe) dating database is available for the axial part of the orogen [*Thomson et al*., 2010; *Guillaume et al*., 2013; *Folguera et al*., 2015]. However, such type of data are completely lacking from the broken foreland area. Yet this has experienced major tectonic events during Andean orogenesis [*Echaurren et al*., 2016]. In this study, we integrate field structural observations with new AHe data in the Esquel-Gastre area (located at latitudes 41°30′–43°S) in order to analyze and compare the exhumation patterns from the frontal part of the orogen and from the adjacent foreland sector and then use them to gain new insights into the timing and modes of coupling versus uncoupling of the deformation between the northern Patagonian fold and thrust belt and its foreland.

2. Geological Setting

The southern Andes is a roughly linear orogenic belt produced by the convergence between the Nazca and Antartic plates beneath the South American plate. The building of the present-day orogen has been interpreted as a result of a series of shortening pulses that took place since the Late Cretaceous [*Folguera and Ramos*, 2011]. Despite the general along-strike continuity of the mountain belt, its internal tectonic segmentation is marked by the variable position of the magmatic arc and of the deformation front in the retroarc area to the east. Thus, this plate margin results in a more complex configuration with respect to the simplified notion of "Andean-type" subduction system proposed in the past literature [e.g., *Gutscher*, 2002]. Marked variations in convergence rates have been calculated from continuous-GPS measurements and NUVEL-1 models along the chain. These measurements unraveled relatively high convergence rates (between 6 and 7 cm/yr) in the Nazca-South America sector and lower ones (less than 2 cm/yr) where the Antarctic plate sinks beneath South America [*Gripp and Gordon*, 1990; *DeMets et al*., 1990; *Kendrick et al*., 1999].

The area of this study is located between latitudes 41°30′ and 43°S, where the Andean orogen is constituted by a series of morphotectonic elements including, from west to east [e.g., *Orts et al*., 2015] (Figures 1b and 2), (i) the Coastal Cordillera, (ii) the Chilean Central Valley, (iii) the northern Patagonian Cordillera, and (iv) the foreland. The Carboniferous-Triassic units of the Coastal Cordillera, which were deformed during the Gondwanian orogenic cycle, are partly covered by Mesozoic-Cenozoic strata [*Thomson and Hervé*, 2002; *Willner et al*., 2004; *Orts et al*., 2015]. The Chilean Central Valley, representing the forearc region, hosts a series of Eocene to Quaternary basins filled by volcaniclastic, marine, and continental deposits [*González*, 1989; *Radic et al*., 2009]. This area was affected by intense subsidence interpreted as resulting from subduction erosion in early Miocene times (~17 Ma), leading to a Pacific-derived transgression with the deposition of deep marine sediments [*Encinas et al*., 2012]. The northern Patagonian Cordillera includes large Quaternary

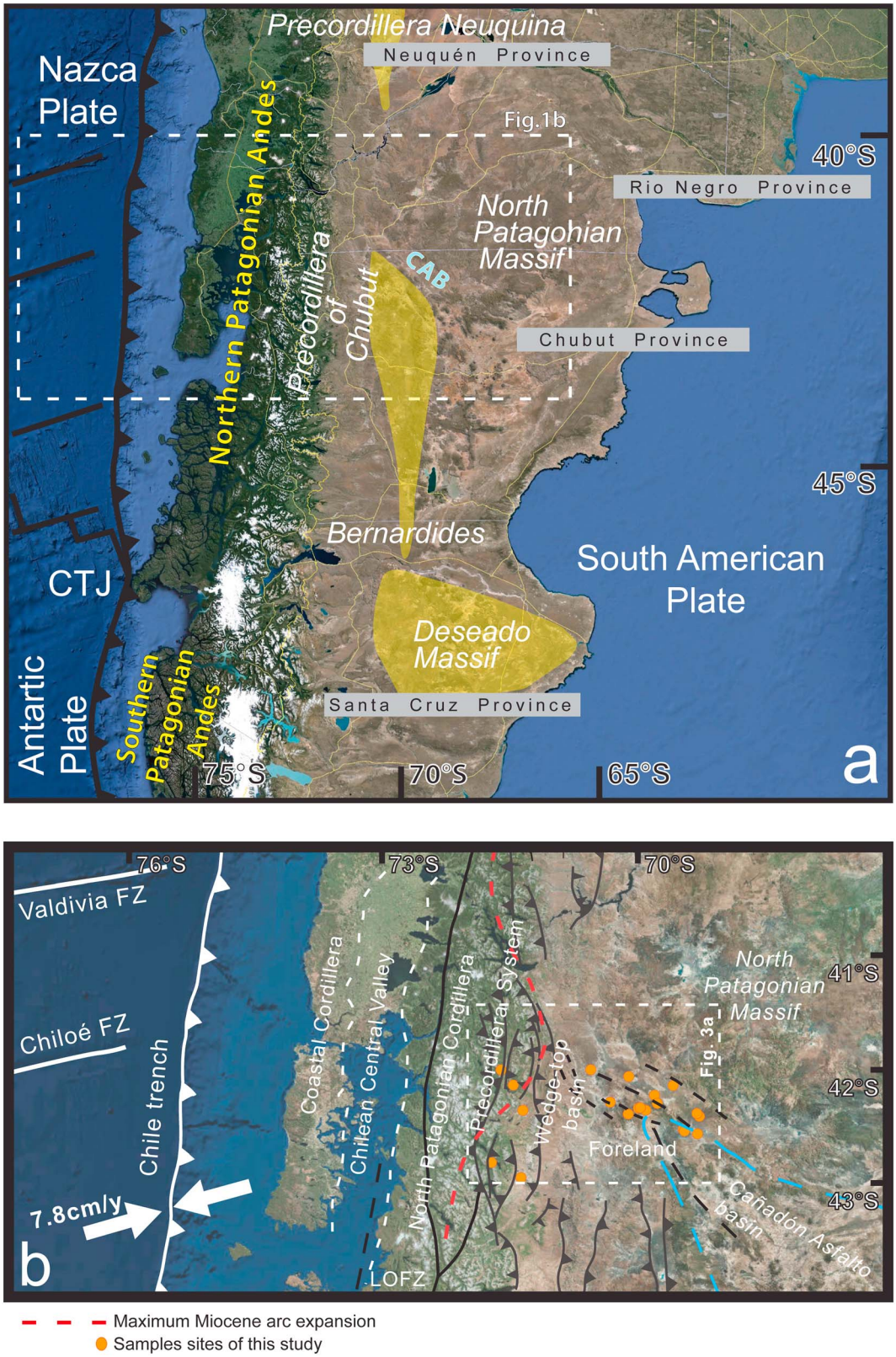

Figure 1. (a) Present tectonic setting of North and Central Patagonia, showing administrative provinces, major tectonic features of the region, and location of Figure 1b. Yellow shaded areas represent deformed foreland sectors; CAB: Cañadón Asfalto Basin, CTJ: Chile Triple Junction. (b) Structural sketch map showing main morphotectonic units and structures of the Andes and adjacent foreland between 40° and 44°S, sampling sites of this study, and location of the geological map of Figure 3.

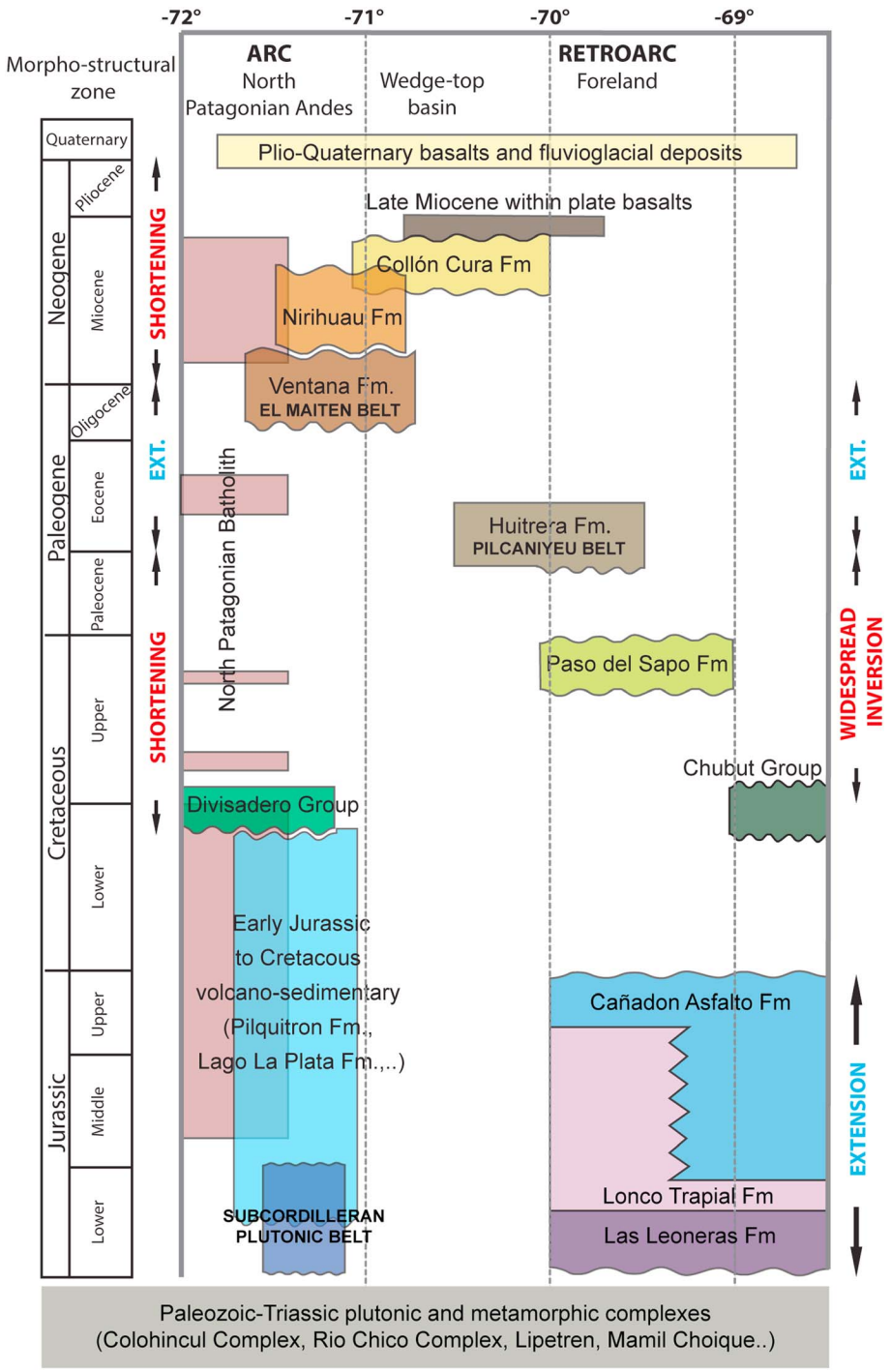

Figure 2. Stratigraphic correlations, main magmatic bodies, and tectonic regimes characterizing the various morphostructural domains of the study area.

stratovolcanoes representing the recent volcanic arc [*Stern*, 2004] and underlying Neogene-Mesozoic volcaniclastic successions. These, in turn, rest on top of the North Patagonian Batholith, which is a ~ 2000 km long and 120 km wide (on average) plutonic body parallel to the Pacific coastline, with associated smaller satellite intrusions spread along both western and eastern Andean slopes [*Orts et al.*, 2015, and references therein]. North to the Chilean Triple Junction, the North Patagonian Batholith includes Middle Jurassic to Miocene rocks of calc-alkaline composition [*Castro et al.*, 2011; *Pankhurst et al.*, 1999] intruding the

Upper Paleozoic basement. In this sector the Liquiñe-Ofqui Fault Zone is a major transpressional intra-arc fault system (Figure 1b) that accommodates the oblique convergence between the Nazca and South America plates and along which most of the Quaternary volcanism and faulting develop [*Hervé*, 1994; *Cembrano et al*., 1996; *Rosenau et al*., 2006; *Vargas Easton et al*., 2013]. This is an ~ 1000 km long strike-slip fault characterized by dextral motion during the Cenozoic, when it was active within the arc roots in a thermally weakened crust [*Cembrano et al*., 1996; *Lavenu and Cembrano*, 1999; *Thomson et al*., 2010], and by previous left-lateral motion during the Mesozoic, when it favored the emplacement of the Patagonian Cordilleran Batholith [*Cembrano et al*., 1996; *Castro et al*., 2011]. East of the Liquiñe-Ofqui Fault Zone, the northern Patagonian Cordillera is characterized by a thick-skinned style of thrusting. During Cretaceous-late Paleogene and Neogene shortening phases [*Giacosa et al*., 2005; *Homovc et al*., 2011; *Orts et al*., 2012; *Ramos*, 1981; *Ramos and Cortés*, 1984], this type of deformation produced the exhumation of the North Patagonian Batholith and of the igneous-metamorphic basement. Thick-skinned thrusting is related with the reverse fault reactivation of preexisting normal faults and is accompanied by basin inversion [*Giacosa and Heredia*, 2004a]. Reactivated normal faults were originally related with two main extensional stages in the study area: (i) an Early to Middle Jurassic preorogenic stage, accompanied by the accumulation of volcano-sedimentary units in the northern Patagonian Cordillera (Piltriquitrón Formation and equivalents), where interbedded tuff and sedimentary strata were dated as ~197–192 Ma old by U/Pb zircon dating [*Orts et al*., 2012; *Spalletti et al*., 2010] and (ii) an Oligocene to early Miocene intraorogenic stage associated with the occurrence of the El Maitén magmatic belt [*Rapela et al*., 1988]. The latter would be related to a regional episode of intra-arc extension affecting the whole Southern Central Andes [*Charrier et al*., 2002; *Godoy et al*., 1999; *Jordan et al*., 2001; *Radic et al*., 2002]. Across the northern Patagonian Andes, these volcanic rocks, interbedded with marine and continental sedimentary rocks [*Cazau et al*., 1989; *Ramos*, 1982], have been related to extensional processes, based on geochemistry and structural evidence [*Aragón et al*., 2011; *Bechis and Cristallini*, 2006; *Bechis et al*., 2014; *Giacosa and Heredia*, 2004b; *Rapela et al*., 1988]. This extensional stage has been unraveled also in the foreland by *Mancini and Serna* [1989].

Early Cretaceous volcanics of calc-alkaline affinity, forming the Divisadero Group [*Skármeta and Charrier*, 1976; *Ramos*, 1981; *Rapela et al*., 1988; *Suárez et al*., 1996; *Suárez and De La Cruz*, 2001], cover Jurassic successions and older intrusive rocks in the eastern parts of the northern Patagonian Cordillera. The frontal eastern foothill area, also termed "Precordilleran System" [e.g., *Orts et al*., 2015], is dominated by Paleozoic basement intruded by the Early Jurassic Subcordilleran Plutonic Belt [*Gordon and Ort*, 1993]. These rocks are covered by roughly coeval volcano-sedimentary successions that were deposited in a NNE trending intra-arc extensional system [*Giacosa and Heredia*, 2004b; *Orts et al*., 2012]. In this region, two Cenozoic magmatic belts developed, related to extensional intraorogenic events [*Giacosa and Heredia*, 2004a]. The Paleocene to Eocene Pilcaniyeu magmatic belt is characterized by bimodal volcanic rocks ranging from predominant rhyolithic ignimbrite facies to subordinate andesites and basalts [*Mazzoni et al*., 1991; *Rapela et al*., 1988]. To the east, the previously mentioned El Maitén magmatic belt (late Oligocene-early Miocene) is characterized by widespread outcrops of andesites and dacitic ignimbrites with subordinate basaltic lava flows and rhyolitic ignimbrites. These two magmatic belts are affected by Cenozoic folds [*Ramos et al*., 2011; *Morabito and Ramos*, 2012; *Bilmes et al*., 2013]. Tertiary shortening is particularly well documented by both foreland basin and wedge-top basin synorogenic deposits, which preserve progressive unconformities and effectively record depocenter migration during the Miocene [*Ramos et al*., 2011; *Orts et al*., 2012; *Bilmes et al*., 2013; *Echaurren et al*., 2016]. The overlying flat-lying Pliocene-Pleistocene volcanics, classifying as alkali basalts, basanites, and trachybasalts, indicate a within-plate environment that differs from previous Andean arc-magmatic rocks [*Massaferro et al*., 2006].

The north Patagonian foreland to the east is dominated by a landscape of faulted basement blocks and intramontane depressions filled by Neogene-Quaternary clastic and volcanic deposits [*Bilmes et al*., 2013; *Echaurren et al*., 2016]. One of these Neogene-Quaternary depressions, i.e. the Gastre Basin, retraces the Mesozoic rift-related Cañadón Asfalto Basin [*Coira et al*., 1975; *Dalla Salda and Franzese*, 1987; *Bilmes*, 2012]. The boundaries of this basin follow regional NW and NNE trending lineaments [*Coira et al*., 1975]. The pre-Jurassic basement of the Cañadón Asfalto Basin consists of granitoids and metamorphic rocks of Carboniferous to Triassic age [*Duhart et al*., 2002; *Pankhurst et al*., 2006; *von Gosen*, 2009] grouped into several lithostratigraphic units. The Cushamen Formation [*Volkheimer*, 1964] and the Calcatapul Formation [*Proserpio*, 1978] are part of a metamorphic basement that was intruded by plutonic bodies of the El Platero

a

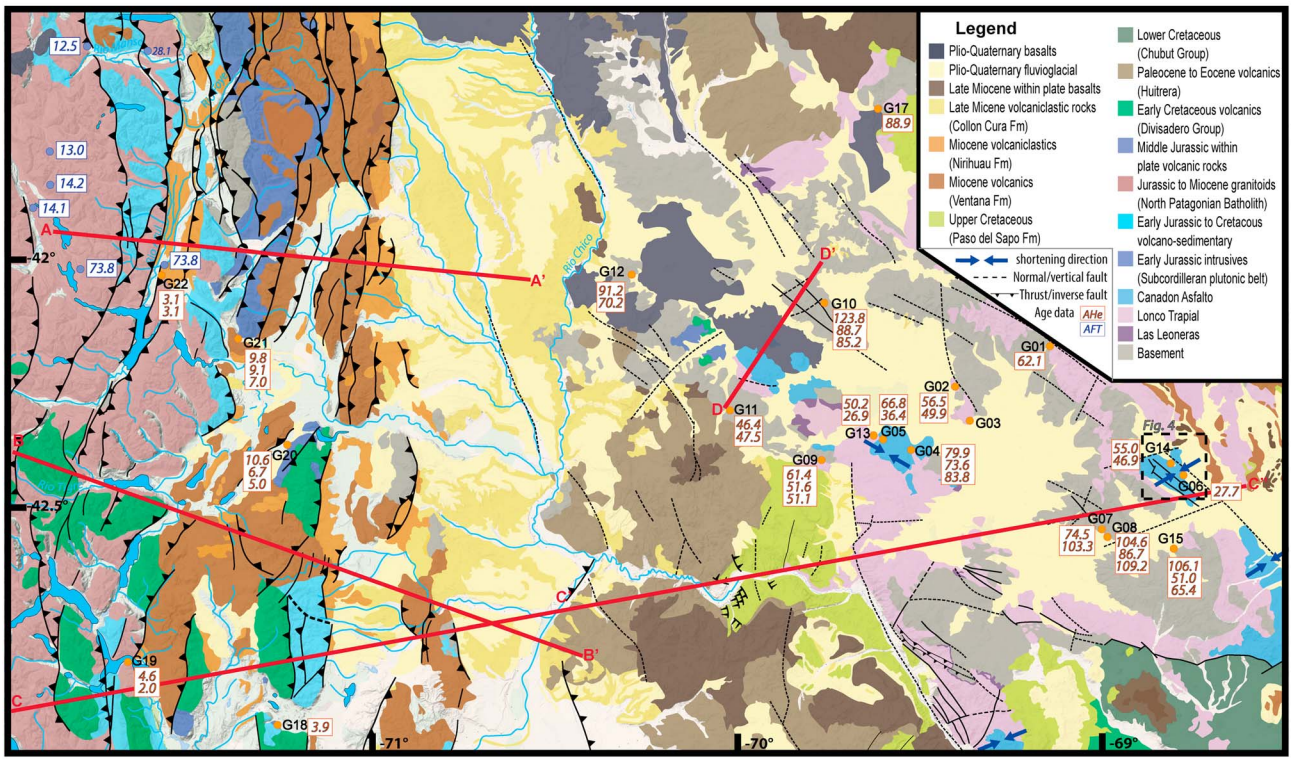
Legend
Plio-Quaternary basalts
Plio-Quaternary fluvioglacial
Late Miocene within plate basalts
Late Micene volcaniclastic rocks (Collon Cura Fm)
Miocene volcaniclastics (Nirihuau Fm)
Miocene volcanics (Ventana Fm)
Upper Cretaceous (Paso del Sapo Fm)
Lower Cretaceous (Chubut Group)
Paleocene to Eocene volcanics (Huitrera)
Early Cretaceous volcanics (Divisadero Group)
Middle Jurassic within plate volcanic rocks
Jurassic to Miocene granitoids (North Patagonian Batholith)
Early Jurassic to Cretacous volcano-sedimentary
Early Jurassic intrusives (Subcordilleran plutonic belt)
Canadon Asfalto
Lonco Trapial
Las Leoneras
Basement
shortening direction
Normal/vertical fault
Thrust/inverse fault
Age data AHe AFT
Fig. 4
-42°
-42.5°
-71°
-70°
-69°

b

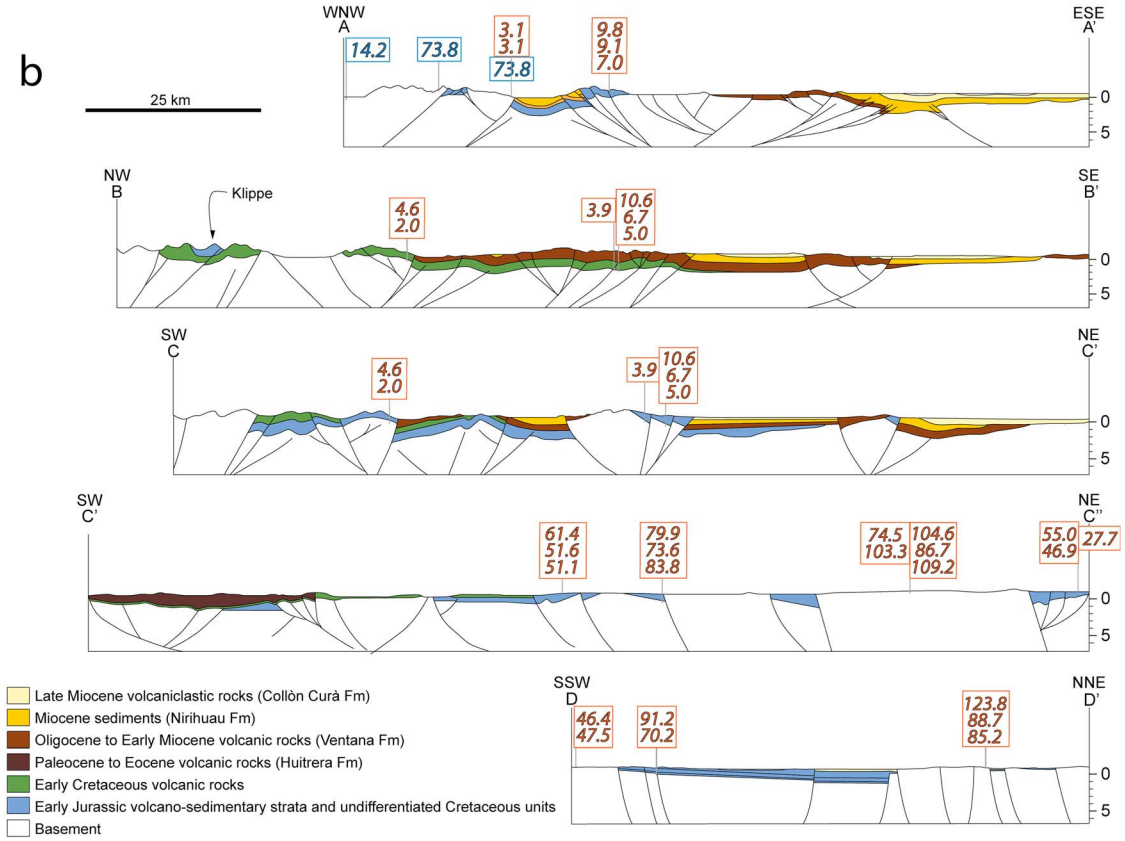
25 km
WNW A
ESE A'
NW B
Klippe
SE B'
SW C
NE C'
SW C'
NE C''
SSW D
NNE D'
Late Miocene volcaniclastic rocks (Collòn Curà Fm)
Miocene sediments (Nirihuau Fm)
Oligocene to Early Miocene volcanic rocks (Ventana Fm)
Paleocene to Eocene volcanic rocks (Huitrera Fm)
Early Cretaceous volcanic rocks
Early Jurassic volcano-sedimentary strata and undifferentiated Cretaceous units
Basement

Formation [*Volkheimer*, 1964], the Mamil Choique Formation [*Ravazzoli and Sesana*, 1977] and the Lipetrén Formation [*Ravazzoli and Sesana*, 1977]. The Jurassic-Lower Cretaceous Cañadón Asfalto extensional basin included nonmarine, normal fault-bounded isolated depocenters that were partially inverted during the Cretaceous [*Allard et al*., 2011; *Folguera and Ramos*, 2011]. In the study area, the infill of the Cañadón Asfalto Basin includes the Early Jurassic Las Leoneras and Lonco Trapial Fms. (radiometrically dated using the zircon Pb/U method by *Cúneo et al*. [2013]) and the Toarcian to Middle-Late Jurassic Cañadón Asfalto Formation (Pb/U ages of 178.8 ± 0.1 Ma and 157.4 ± 0.6 Ma) [*Cúneo et al*., 2013]. The Cañadón Asfalto Basin has an economic relevance because it hosts the epithermal world-class polymetallic Ag + Pb (Cu, Zn) Navidad deposit, with resources of 19.670 t Ag; 1,320,000 t Pb; and significant contents of Cu and Zn in eight separate to semicontinuous deposits [*Williams*, 2010]. The Jurassic to Lower Cretaceous succession is unconformably overlain by the Upper Cretaceous to Paleocene marine and continental deposits of the Paso del Sapo and Lefipán Fms. [*Lesta and Ferello*, 1972]. These units, representing the record of the Campanian-Danian transgression [*Spalletti and Dalla Salda*, 1996], are covered by an Eocene volcanic succession [*Cazau et al*., 1989] including andesites, dacites, and rhyolites of the Huitrera Formation [*Ravazzoli and Sesana*, 1977]. Stratigraphically overlying Neogene-Quaternary continental deposits are preserved within tectonic depressions (such as the Gastre Basin) and, to a lesser extent, on top of the uplifted fault-bounded blocks.

3. Structural Constraints From the Gastre-Navidad Area

The map-scale structure of the Gastre-Navidad area (Figures 3a and 4) is dominated by high-angle faults. Pre-Mesozoic units record internal deformation produced by NE-SW shortening, accompanied by lower greenschist facies metamorphism [*von Gosen and Loske*, 2004]. Map-scale folds are locally well developed in the Mesozoic-Tertiary successions, particularly in the Cañadón Asfalto Fm. Examples of outcrop structural features from the Cañadón Asfalto Fm are shown in Figure 5, while orientation data are provided in Figure 6.

The Cañadón Asfalto Fm. is affected by two sets of faults, striking dominantly NW-SE and NE-SW (Figures 6a and 6b), often recording a synsedimentary/syndiagenetic extensional activity documented by sediment thickness variations across the faults, disruption of not yet completely lithified beds (Figures 5a and 5b), and carbonate sediment filling of dilatant structures (hybrid dilation/shear fractures). About 30% of these faults—arguably syndiagenetic in origin—preserve kinematic indicators in the form of striae and/or mineral (dominantly calcite) shear fibers on slickenside surfaces. When slickenlines were present, their pitch has been measured together with sense of shear. These data (Figure 6c) have been used to obtain information on the strain field controlling the development of the fault set, using the *P-B-T* technique [*Angelier and Mechler*, 1977]. The *P-B-T* method, based on plane orientation, slip orientation, and kinematics of each single fault, furnishes the three principal axes of strain: *P* (direction of maximum shortening), *T* (direction of maximum stretching), and *B* (intermediate axis, orthogonal to the *P-T* plane). In order to calculate the orientation of each strain axis, this method uses a common defined fracture angle θ for all fault-slip data. *P-B-T* axes were determined using FaultKin v.7.4.3 software [*Marrett and Allmendinger*, 1990; *Allmendinger et al*., 2012], which utilizes the right dihedra geometrical method of paleostress analysis of *Angelier and Mechler* [1977] and *Pfiffner and Burkhard* [1987] (for small-offset faults such as those analyzed in this study, and accepting the Wallace-Bott hypothesis that the slip is parallel to the resolved shear stress [*Wallace*, 1951; *Bott*, 1959], the obtained strain axes can be assumed to approximate infinitesimal strain and therefore to represent paleostress principal axes). The analysis unraveled an extensional tectonic regime characterized by a subvertical *P* axis and a subhorizontal, SW-NE trending *T* axis (Figure 6d).

Figure 3. (a) Geological map of the study area (based on *Ardolino et al*. [2009], *Lizuaín* [2009], *Lizuaín and Silva Nieto* [2011], *Orts et al*. [2012], *Bilmes et al*. [2013], and *Orts et al*. [2015], integrated with our own field mapping). New apatite (U-Th)/He ages from our samples (G01 to G22; error of 10% at 1σ has to be considered for AHe ages) are shown together with published apatite fission track (AFT) ages [from *Thomson et al*., 2010]. Shortening directions were obtained based on the analysis of the layer-parallel shortening-related structural assemblage (consisting of pressure solution cleavage, veins, and conjugate faults). (b) Cross sections [from *Bilmes et al*., 2013; *Orts et al*., 2015; *Echaurren et al*., 2016], showing projected low-temperature thermochronometric data. As pointed out by the original authors of these geological sections, the structure is dominated by reverse-slip reactivation of preexisting normal faults. Depending on the degree of tectonic inversion, faults may show variable reverse/normal fault separation at different stratigraphic levels. The thickness of the stratigraphic units can also change between footwall and hanging wall blocks of original, synsedimentary normal faults.

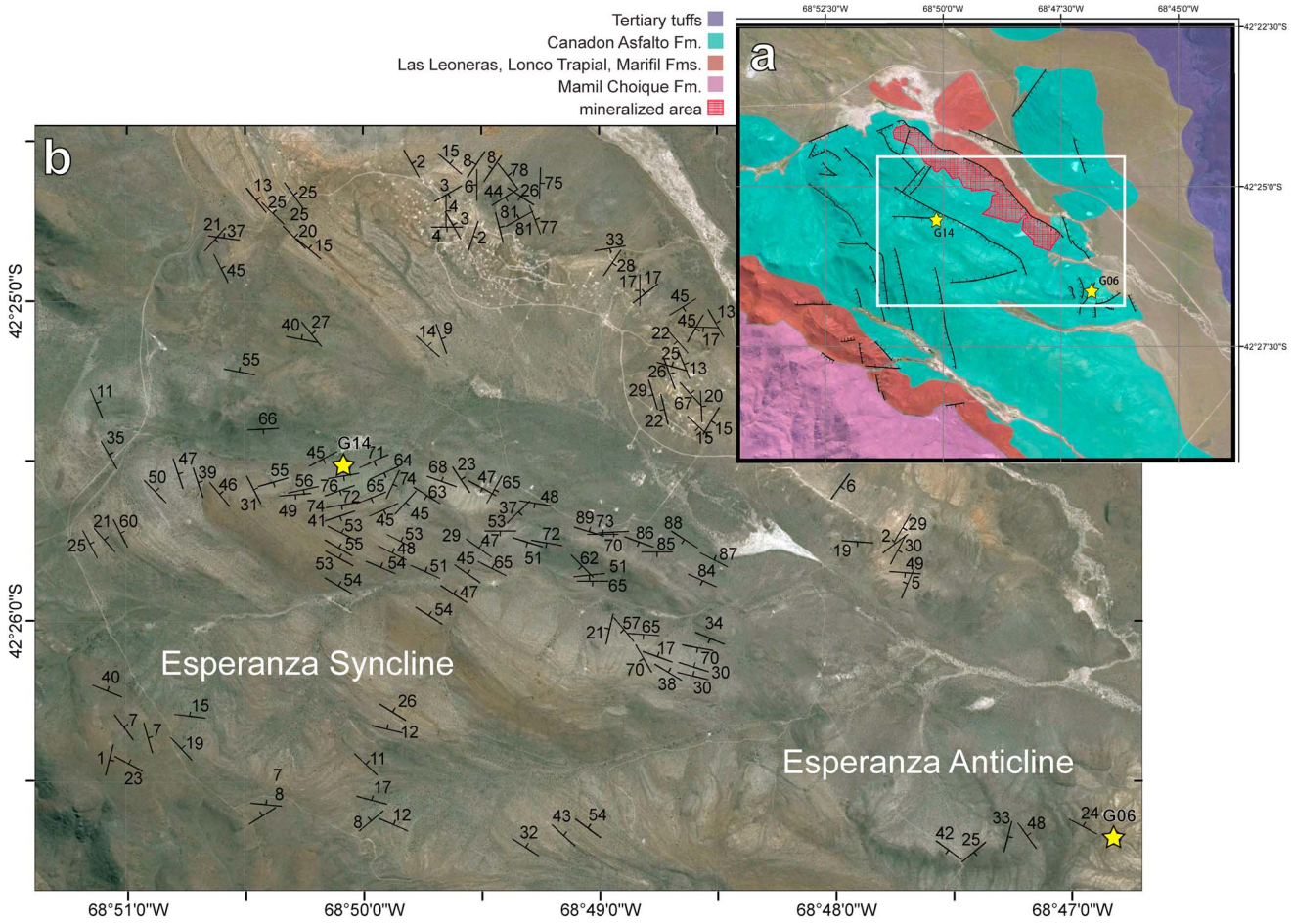

Figure 4. (a) Geological map of the Navidad Project (modified after *Williams* [2010]), showing location of samples collected in the ore deposit area and (white box) that of the satellite image reporting bedding data gathered in the (b) folded zone of Navidad.

Hydrothermal veins, up to tens of centimeters thick and mainly composed of barite (Figure 5c), also occur as dominant NW-SE and NE-SW striking sets (Figures 6e and 6f). This whole composite fault-vein system appears to control the mineralization in the ore deposit of Navidad, which can be confidently ascribed to the Mesozoic (Jurassic), as already suggested by *Williams* [2010].

The analysis of bedding data from the Cañadón Asfalto Fm. indicates that this is dominated by subhorizontal to gentle dips, although folding is clearly recorded by the distribution of poles to bedding (Figures 6g and 6h). Bedding attitudes record folding of the Cañadón Asfalto Fm. around a subhorizontal statistical axis at a regional scale. The analysis of bedding distribution around single folds (e.g., Esperanza Syncline and Esperanza Anticline in Figure 4) shows how adjacent individual structures may be characterized by slightly different mean axial trends (Figures 6i–6l). These folds are clearly the result of shortening of the sedimentary succession, as testified by tectonic stylolites (i.e., spaced pressure solution cleavage) at a high angle to bedding in limestones (Figure 5f), the bedding-cleavage intersection being roughly parallel to the local fold axis. Calcite-filled extension veins occur perpendicular to the tectonic styolites. The two sets of shortening and extension structures show mutually crosscutting relationships, indicating that they are essentially coeval. Small normal faults also strike parallel to the extension veins. The tension gashes are parallel to the acute bisector of conjugate normal faults, thus suggesting that these features form part of a single structural association. The whole cleavage-vein-normal fault structural assemblage records mutually orthogonal horizontal maximum (σ_1) and minimum (σ_3) compression during layer-parallel shortening preceding fold amplification, a stress configuration that is typical of prethrusting foreland shortening [*Tavani et al.*, 2015] and is also consistent with the evidence of syncontractional, perpendicular extension in the foreland of the Patagonian Andes at a more regional scale [*Gianni et al.*, 2015a]. The layer-parallel shortening-related structural

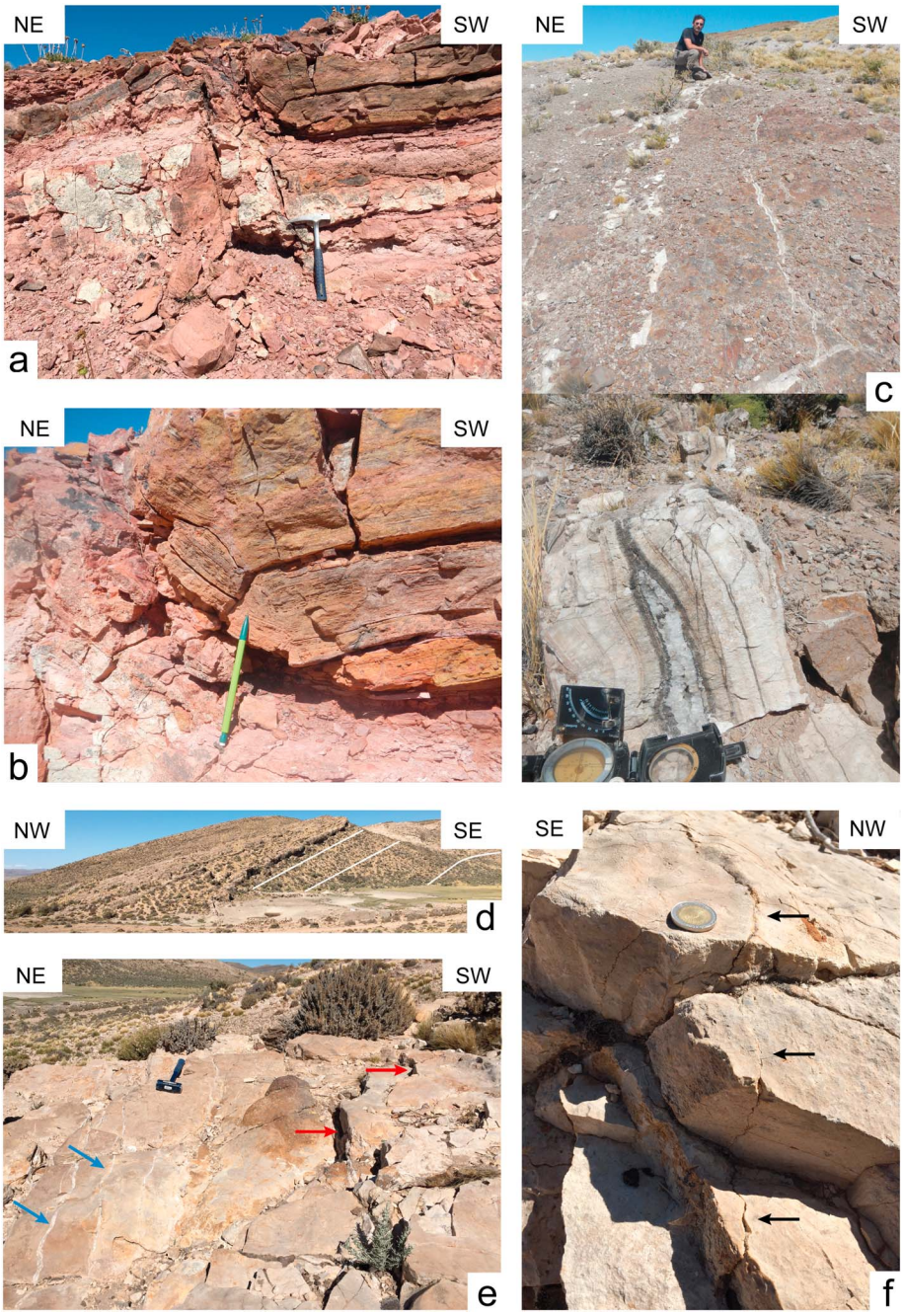

Figure 5. Examples of outcrop structures from the Cañadón Asfalto Fm. (a) Jurassic minor fault showing silicified fault core testifying hydrothermal circulation (Navidad area). (b) Detail of fault hanging wall from Figure 5a, showing folded and partially disrupted laminated bed. (c) Barite-bearing hydrothermal veins (Navidad area). (d) NW dipping fold limb in Upper Jurassic limestone beds (about 30 km WSW of Gastre). (e) Outcrop of Upper Jurassic limestone beds on NW dipping fold limb of Figure 5d, showing NW striking calcite-filled extension veins (blue arrows) normal to bedding and minor normal faults (red arrows) at a high angle to bedding. (f) Detail of previous outcrop, showing NE striking spaced pressure solution cleavage surfaces (arrowed) normal to bedding.

assemblage has been used to obtain shortening directions for various sites within the study area (displayed in Figure 3a). Although bedding data are somewhat dispersed (Figures 6g–6l), individual folds are relatively simple, subcylindrical [*Ramsay and Huber*, 1987] structures accompanied by a single generation of related cleavage. Therefore, variable fold trends appear not to be the result of superposed folding events. Rather, it may envisaged that shortening of the Cañadón Asfalto Basin occurred by buttressing of the sedimentary

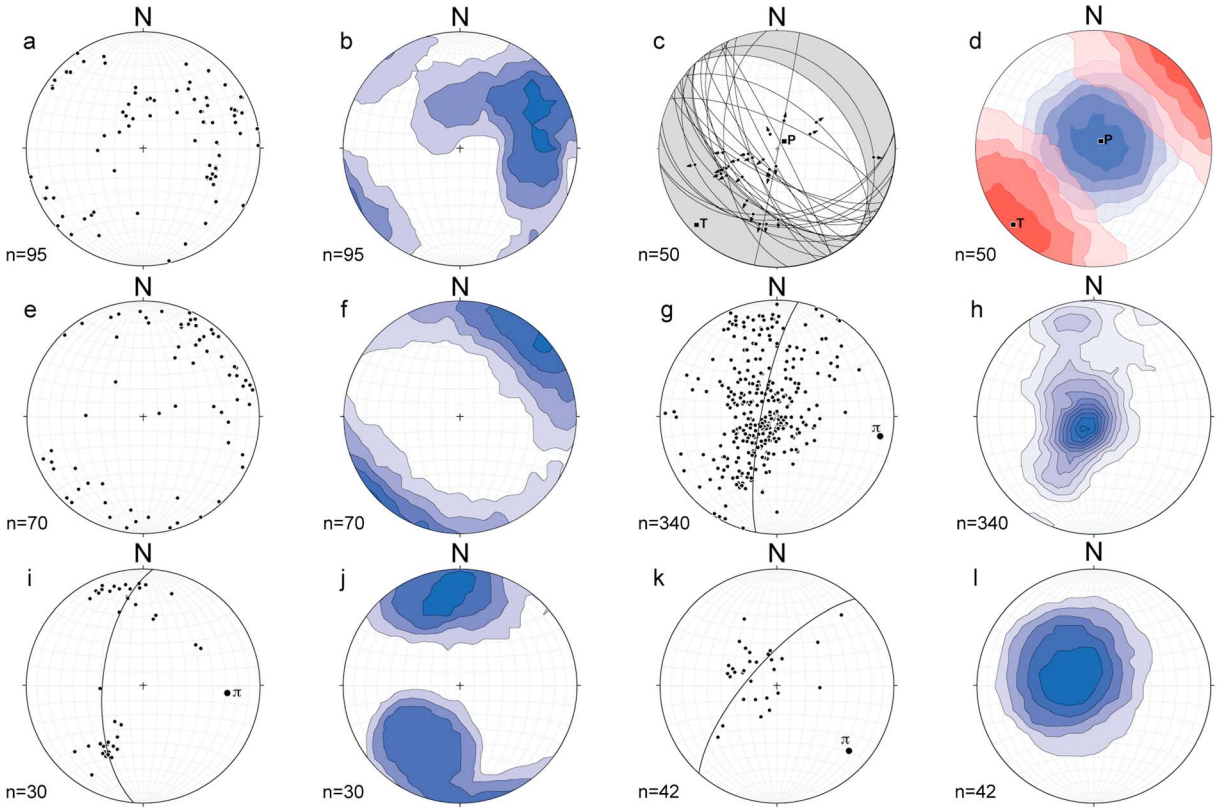

Figure 6. Orientation data (lower hemisphere, equal area projections of poles to planes drawn using Stereonet v.9.5.1 software) [*Allmendinger et al*., 2012; *Cardozo and Allmendinger*, 2013] for the Gastre area. All contours are drawn using the Kamb method with intervals at 2σ and significance level of 3σ. (a) Extensional faults showing evidence of synsedimentary/syndiagenetic activity. (b) Contour plot of data shown in Figure 6a. (c) Subset of the fault population plotted in Figure 6a, showing faults preserving slickenlines (arrows) and reliable shear sense indicators. Fault plane solution obtained by kinematic analysis performed with FaultKin v.7.4.3 software [*Marrett and Allmendinger*, 1990; *Allmendinger et al*., 2012] is also shown (grey shaded "beach ball"). (d) Contours of *P* (blue) and *T* (red) axes obtained from the kinematic analysis shown in Figure 6c. (e) Hydrothermal veins. (f) Contour plot of data shown in Figure 6e. (g) Bedding in the Cañadón Asfalto Fm. (h) Contour plot of data shown in Figure 6g. (i) Bedding from the Esperanza Syncline (refer to Figure 3). (j) Contour plot of data shown in Figure 6i. (k) Bedding from the Esperanza Anticline (refer to Figure 3). (l) Contour plot of data shown in Figure 6k. For diagrams in Figures 6g, 6i, and 6k, the best fit great circle approximating data distribution is shown, together with its pole (π) representing the statistical fold axis.

infill against basement blocks representing the footwall of Mesozoic rift-related normal faults, thus resulting in variable fold trends being controlled by the inherited, complex basin architecture. This style of shortening and the related variability of maximum shortening directions (Figure 3a) are consistent with the tectonic inversion already documented for this foreland sector, which is termed broken foreland because of this type of deformation dominated by double-vergent structures controlled by the reactivation of preexisting normal faults [e.g., *Folguera and Ramos*, 2011; *Orts et al*., 2012, 2015] (refer to the cross sections in Figure 3b).

4. Apatite (U-Th)/He Thermochronometry

In order to analyze and compare the tectonic evolution and exhumation of the frontal part of the east vergent northern Patagonian Andes and of the adjacent foreland, a transect has been selected from the eastern slope of the Cordillera to the area of the Gastre Basin (reaching a longitude of ~ 68.5°W), thereby including the Navidad silver deposit.

4.1. Materials and Methods

Collected samples can be included into two main groups (see Table 1 for details). A first group comprises the samples gathered from the foreland area. Samples G01, G02, G04, G07, G08, G10, G11, G12, G15, and G17 were collected from basement rocks cropping out in uplifted fault blocks bounding the Gastre Basin (Figure 3a). These granitoid samples are from the Lipetren Fm. (Lower Paleozoic) and the Mamil Choique

Table 1. Sample Location (With Formation and Stratigraphic Age)

Sample Name	Coordinates		Elevation	Lithology	Formation	Stratigraphic Age
	Latitude	Longitude				
G01	42°11′34″	69°09′56″	1134	Granite	Lipetren	(Permo-)Triassic
G02	42°15′57″	69°24′31″	929	Granite	Mamil Choique	Lower Paleozoic to Lower Permian
G03	42°20′17″	69°22′32″	958	Granite	Lipetren	(Permo-)Triassic
G04	42°23′16″	69°31′19″	997	Granite	Mamil Choique	Lower Paleozoic to Lower Permian
G05	42°22′10″	69°37′45″	963	Conglomerate	Cañadón Asfalto	Upper Jurassic
G06	42°26′40″	68°46′49″	1150	Arkose	Cañadón Asfalto	Upper Jurassic
G07	42°33′35″	69°00′14″	1070	Granite	Mamil Choique	Lower Paleozoic to Lower Permian
G08	42°33′50″	69°00′15″	1043	Granite	Mamil Choique	Lower Paleozoic to Lower Permian
G09	42°24′47″	69°46′56″	995	Arkose	Cañadón Asfalto	Upper Jurassic
G10	42°05′43″	69°46′30″	1060	Granite	Mamil Choique	Lower Paleozoic to Lower Permian
G11	42°18′41″	70°02′12″	999	Granite dyke	Mamil Choique	Lower Paleozoic to Lower Permian
G12	42°02′07″	70°17′57″	976	Granite	Mamil Choique	Lower Paleozoic to Lower Permian
G13	42°22′25″	69°36′14″	973	Sandstone	Cañadón Asfalto	Upper Jurassic
G14	42°25′31″	68°50′05″	1177	Sandstone	Cañadón Asfalto	Upper Jurassic
G15	42°35′10″	68°48′46″	1103	Granite	Mamil Choique	Lower Paleozoic to Lower Permian
G16	42°35′18″	69°44′05″	534	Sandstone	Passo del Sapo	Upper Cretaceous
G17	41°42′43″	69°37′09″	1275	Granite	Mamil Choique	Lower Paleozoic to Lower Permian
G18	42°55′50″	71°15′38″	617	Granite	Subcordilleran Plutonic Belt	Lower Jurassic
G19	42°48′23″	71°39′39″	576	Granitoid	Batolite Patagonico	Upper Cretaceous
G20	42°23′05″	71°14′43″	663	Granite	Leleque	Upper Jurassic
G21	42°10′02″	71°21′26″	616	Granodiorite	Subcordilleran Plutonic Belt	Lower Jurassic
G22	42°01′49″	71°34′34″	275	Granite	Batolite Patagonico	Upper Cretaceous

Fm. (Permo-Triassic). Samples G5, G6, G9, G13, and G14 were collected from the Cañadón Asfalto Fm. (Upper Jurassic). In particular, samples G6 and G14 are from the ore deposit district of Navidad. A second group of samples (G18, G19, G20, G21, and G22) includes those gathered in the western part of the study area, from the Leleque and El Maiten Ranges, constituting the frontal part (i.e., the so-called Precordillera System) of the northern Patagonian Andes.

(U-Th)/He (AHe) ages have been obtained from carefully selected apatite grains with a minimum width of 60 μm, which have been measured along the two axes on two faces and then placed into a Niobium basket. One to three replicates have been analyzed per sample. Sphere equivalent radius, weight, and ejection factors have been determined, assuming a homogeneous distribution of U and Th in apatite, using dedicated software [*Gautheron and Tassan-Got*, 2010; *Ketcham et al*., 2011; *Gautheron et al*., 2012]. The Niobium baskets have been heated twice using a diode laser at 1030 ± 50°C for 5 min, allowing for total He degassing and to check the presence of He trapped in small inclusions (see *Fillon et al*. [2013] for more details). After He extraction, Nb baskets were placed into a single-used polypropylene vials. Apatite grains were dissolved for 3 h at 70°C in a 50 μL HNO_3 5 N¬ solution containing a known content of ^{235}U, ^{230}Th, and ^{149}Sm, and additional 50 μL HNO_3 5 N and then filled with 0.9 mL of ultrapure MQ water. The final solution was measured for U, Th, and Sm concentrations by quadrupole inductively coupled plasma (ICP)-quadrupole mass spectrometry (CCT Thermo-Electron at LSCE (Gif/Yvette; France). The analysis was calibrated using external age standards, including Limberg Tuff and Durango apatites. A mean AHe age of 16.0 ± 1.4 Ma and 31.1 ± 2.1 Ma has been measured for the Limberg Tuff and yellow Durango apatite, which are in agreement with published data (i.e., 16.8 ± 1.1 Ma and 31.0 ± 1.0) [*Kraml et al*., 2006; *McDowell et al*., 2005]. An error at 10% at 1σ should be considered, reflecting the sum of ejection factor F_T correction and standard dispersion. The HeFTy software [*Ketcham*, 2005] was used to generate an inverse thermal modeling based on AHe data of four representative samples (G07, G13, G15, and G22), in order to test plausible thermal histories. We chose three samples belonging to the broken foreland area, for which there is a complete lack of low-T thermochronological studies, and one from the Precordillera. Two to three AHe replicates were used for each modeled sample. The RDAAM model of *Flowers et al*. [2009] was adopted for the calibration of kinetic parameters, and *Ketcham et al*. [2011] was considered for the approximation of stopping distances. However, similar results would have been obtained by the use of the damage and annealing model from *Gautheron et al*. [2009]. Surface temperature was assumed to be 10°C. The only constrains used were the following: (i) temperatures between 0 and

Table 2. Apatite (U-Th-Sm)/He Analytical Data[a]

Sample Name	R_s (μm)	Weight (μg)	F_T	^{4}He (nncc/g)	U (ppm)	Th (ppm)	^{147}Sm (ppm)	eU (ppm)	Th/U	Raw AHe Age (Ma)	Corrected AHe Age (Ma)
G01-02	38	1.7	0.64	481,259.6	91	31	151	98	0.3	40.0	62.1 ± 5.6
G02-02	41	1.8	0.72	159,254.4	18	59	82	32	3.3	40.6	56.5 ± 5.1
G02-03	35	0.9	0.66	70,897.9	9	20	486	14	2.2	33.0	49.9 ± 4.5
G04-01	53	3.8	0.79	204,917.2	21	22	66	27	1	62.7	79.9 ± 7.2
G04-02	41	1.4	0.71	257,276.9	32	33	97	40	1	51.9	73.6 ± 6.6
G04-03	44	1.6	0.68	729,467.2	83	96	17	105	1.2	57.3	83.8 ± 7.5
G05-01	50	2.9	0.79	268,589.4	45	46	75	56	1	39.5	50.2 ± 4.5
G05-03	46	1.8	0.75	116,142.7	43	20	65	47	0.5	20.1	26.9 ± 2.4
G06-03	55	3.5	0.78	70,495.9	22	19	66	27	0.9	21.6	27.7 ± 2.5
G07-01	52	2.6	0.73	1,256,944.8	134	3	152	135	0	76.5	104.6 ± 9.4
G07-02	43	2.2	0.68	473,128.2	65	3	106	66	0.1	58.8	86.7 ± 7.8
G07-03	55	3.4	0.75	1,587,006.9	159	9	66	161	0.1	81.4	109.2 ± 9.8
G08-01	39	1.9	0.69	113,056	15	8	133	17	0.5	51.4	74.5 ± 6.7
G08-03	31	0.9	0.65	245,288.5	26	11	155	29	0.4	66.9	103.3 ± 9.3
G09-01	32	0.5	0.57	260,075.3	33	89	933	54	2.7	35.1	61.4 ± 5.5
G09-02	33	0.9	0.63	124,150	19	50	141	31	2.7	32.3	51.6 ± 4.6
G09-03	43	1.6	0.68	149,903.5	19	67	58	36	3.4	34.6	51.1 ± 4.6
G10-01	90	15.2	0.86	207,920.9	14	7	48	16	0.5	106.5	123.8 ± 11.1
G10-02	77	8.8	0.85	172,830.1	17	6	29	19	0.3	75.1	88.7 ± 8.0
G10-03	60	4.5	0.79	163,455.5	18	7	83	19	0.4	67.6	85.2 ± 7.7
G11-02	38	1.3	0.69	89,896.4	17	22	98	23	1.2	31.8	46.4 ± 4.2
G11-03	43	1.6	0.72	40,621	8	3	114	9	0.4	34.1	47.5 ± 4.3
G12-01	53	3.9	0.78	170,929.5	15	17	104	19	1.1	71.4	91.2 ± 8.2
G12-02	52	3.3	0.76	348,509.6	50	13	159	53	0.3	53.3	70.2 ± 6.3
G13-02	58	3.9	0.8	239,706.7	27	40	51	37	1.5	53.3	66.8 ± 6.0
G13-03	70	7	0.82	28,134.2	3	15	79	7	4.4	30.0	36.4 ± 3.3
G14-01	58	3.9	0.79	291,854.3	35	83	61	56	2.4	43.3	55.0 ± 4.9
G14-03	54	4.1	0.77	357,806.4	64	74	89	82	1.2	36.1	46.9 ± 4.2
G15-01	38	0.9	0.63	180,970.1	10	44	204	21	4.4	67.2	106.1 ± 9.5
G15-02	41	4.1	0.77	26,296.8	3	11	52	5	4.3	39.2	51.0 ± 4.6
G15-03	45	1.6	0.69	65,107.3	5	23	135	11	4.3	44.9	65.4 ± 5.9
G17-03	35	1.1	0.65	206,061	25	13	126	28	0.5	58.1	88.9 ± 8.0
G18-02	47	2.5	0.73	42,608.5	103	83	208	123	0.8	2.8	3.9 ± 0.4
G19-02	42	1.8	0.71	20,037.8	26	95	249	49	3.6	3.3	4.6 ± 0.4
G19-03	39	1.3	0.69	11,635.1	53	61	236	68	1.1	1.4	2.0 ± 0.2
G20-01	42	1.5	0.67	20,451.3	11	50	164	23	4.7	7.2	10.6 ± 1.0
G20-02	36	0.9	0.68	12,081.7	13	33	140	21	2.5	4.5	6.7 ± 0.6
G20-03	51	3.3	0.73	5,681.2	6	24	85	12	3.8	3.7	5.0 ± 0.5
G21-01	20	0.9	0.61	41,763.5	51	25	152	57	0.5	5.9	9.8 ± 0.9
G21-02	37	1.1	0.64	32,364.8	38	30	237	45	0.8	5.8	9.1 ± 0.8
G21-03	44	1.9	0.73	16,467.8	23	14	79	26	0.6	5.1	7.0 ± 0.6
G22-02	45	1.5	0.69	33,055.7	84	185	70	129	2.2	2.1	3.1 ± 0.3
G22-03	46	2	0.73	19,459.8	45	109	127	71	2.4	2.2	3.1 ± 0.3

[a] F_T is the ejection correction factor and R_s is the sphere equivalent radius of hexagonal crystal with the same surface/volume ratio, which are both determined by using a dedicated code [*Gautheron and Tassan-Got*, 2010; *Ketcham et al.*, 2011; *Gautheron et al.*, 2012]. AHe ages are corrected for the F_T factor and an error at 1σ is considered.

20°C during the depositional age for the sedimentary sample (G13) and (ii) temperatures between 0 and 20°C for basement samples (G07 and G15), corresponding to their near-surface exposure during Triassic times (marked by an unconformity followed by the deposition of the volcano-sedimentary succession of the Garamilla Fm.). No constraints were imposed for sample G22, as its intrusion age is much older than the recorded AHe age.

4.2. Results and Thermal Modeling

The determined AHe data for each replicate are reported in Table 2. AHe ages and effective uranium content (eU = U + 0.24 Th) present a broad distribution ranging from 2.0 ± 0.2 to 282.3 ± 25.4 Ma and eU range from low to quite high values (3 to 159 ppm). Most of the samples gave ages that will be considered in the

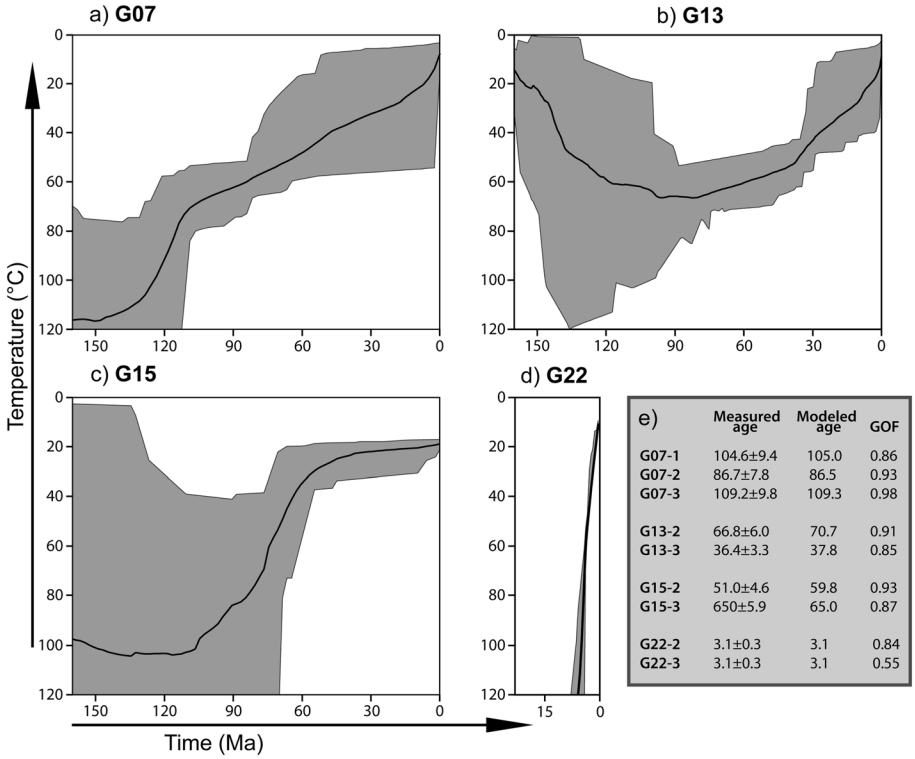

e)	Measured age	Modeled age	GOF
G07-1	104.6±9.4	105.0	0.86
G07-2	86.7±7.8	86.5	0.93
G07-3	109.2±9.8	109.3	0.98
G13-2	66.8±6.0	70.7	0.91
G13-3	36.4±3.3	37.8	0.85
G15-2	51.0±4.6	59.8	0.93
G15-3	650±5.9	65.0	0.87
G22-2	3.1±0.3	3.1	0.84
G22-3	3.1±0.3	3.1	0.55

Figure 7. Thermal modeling (performed with the HeFTy software) [*Ketcham*, 2005] for foreland samples (a) G07, (b) G13, and (c) G15, and (d) Precordilleran sample G22. Good path envelope (supported by the data) and best fitting path are indicated with dark grey areas and a black solid line, respectively. (e) Table summarizing measured age, modeled age, and goodness of fit (GOF) for each considered grain. Age GOF provides an indication of the fit between observed and predicted data (values close to 1 are best).

following discussion. On the other hand, a few replicates have been rejected because they yielded critically high Th/U values, probably due to U or Th-rich (i.e., uraninite or thorite) undetectable inclusions.

The data set presents two different AHe age trends, with a sample group (G18 to 22, sampled along the Precordillera mountain front) characterized by "young" ages (~2 to 10 Ma) and a second one (G1 to 17, sampled in the foreland) characterized by "old" ages (reaching ~110 Ma; Table 2).

The foreland samples, from both Permian-Triassic plutonic rocks and Mesozoic continental sediments of the Cañadón Asfalto Formation, present for a few replicates some dispersion in AHe ages that depends on factors affecting He diffusion kinetics (eU content and crystal size; Figure 8b). This AHe age dispersion reflects a long permanence in the He-Partial Retention Zone (HePRZ). In those conditions, He diffusivity can be different for each grain, implicating closure temperatures ranging from 40 up to 120°C [*Reiners and Farley*, 2001; *Gautheron et al*., 2009; *Flowers et al*., 2009; *Djimbi et al*., 2015]. Based on the AHe data, it may be inferred that the samples from the foreland area stayed in the HePRZ since at least ~110 Ma, with a final exhumation phase at ~30–50 Ma. More information could be extracted from thermal modeling performed using the HeFTy software. Figure 7 shows the possible scenarios of thermal paths experienced by samples G07 and G15 (Mamil Choique Fm.), G13 (Cañadón Asfalto Fm.), and G22 (North Patagonian Batholith). The first two samples consist of Paleozoic basement rocks that, based on stratigraphic constraints [*Lizuaín and Silva Nieto*, 2011], probably experienced burial since ~250 Ma. These two samples show similar path envelopes characterized by a long residence in the HePRZ (between 40 and 80°C), and possibly below it, followed by slow exhumation since ~120 Ma (Figures 7a and 7c). The Cañadón Asfalto sample (G13) experienced a shorter residence after its burial, with subsequent exhumation starting at ~100 Ma (Figure 7b). All these modeled samples do not show any evidence of more recent substantial reheating. On the other hand, the thrust belt samples (G18 to G22), collected from Early Jurassic magmatic rocks of the Subcordilleran Plutonic Belt, show a more recent exhumation phase between 10 Ma and 2 Ma, as indicated also by the thermal modeling performed for sample G22 (Figure 7d).

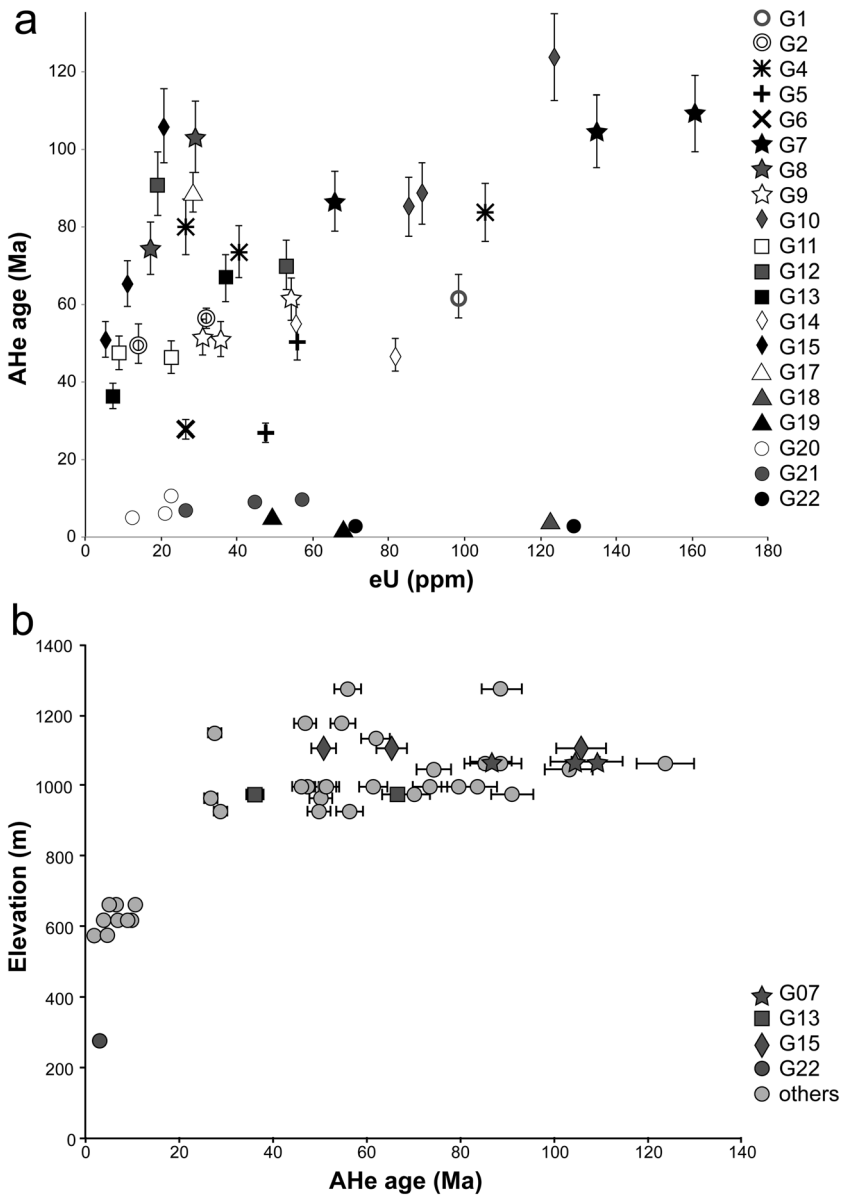

Figure 8. (a) Age-elevation relationships (AERs) for AHe data; samples used for thermal modeling are highlighted. (b) AHe ages plotted against effective uranium concentration (eU = [U] + 0.235 × [Th]).

The long permanence in the HePRZ of some samples is confirmed by the age-elevation relationships (AER; Figure 8a). A first group of data cluster around 650 m of elevation and are characterized by ages younger than 10 Ma. A second subset of ages are localized at elevations between ~ 900 and 1250 m and are characterized by very dispersed ages, spanning from 30 to 120 Ma. The main difference between these two groups of ages can be ascribed to the time spent by the samples in the HePRZ: a rapid cooling though this zone characterized the Precordilleran samples, while a prolonged residence is recorded by the broken foreland samples. In other words, the analyzed foreland area represents a paleo-HePRZ that was brought to surface by exhumation.

5. Discussion

The foreland sector at the latitudes of our study area exposes Late Paleozoic to Jurassic successions that were affected by rifting during Jurassic times [e.g., *Folguera and Ramos*, 2011]. Synsedimentary normal faults and hydrothermal veins, also controlling the mineralization in the Navidad ore deposit, provide a structural record

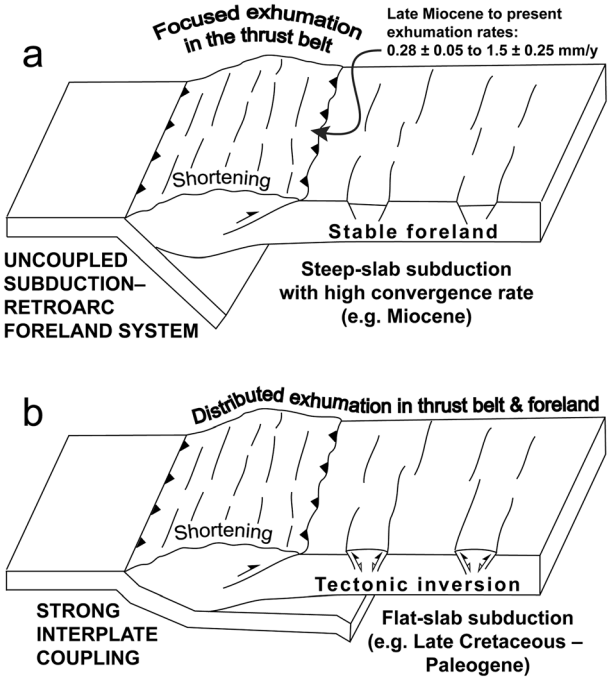

Figure 9. Interpretative cartoon. (a) Uncoupling of the deformation: steep-slab subduction and rollback at high convergence rate produce shortening, tectonic inversion and exhumation in the fold-thrust belt but little or no shortening in the foreland area. (b) Coupling of the deformation: flat-slab subduction produces shortening, tectonic inversion and exhumation over both the fold-thrust belt and the foreland area, leading to the development of the broken foreland.

of such Mesozoic extension in the study area (refer to Figures 5 and 6). Subsequent shortening of this foreland sector has been widely documented [e.g., *Folguera and Ramos*, 2011; *Bilmes et al*., 2013; *Gianni et al*., 2015a, 2015b; *Echaurren et al*., 2016] and has resulted in the folds affecting the succession of the Cañadón Asfalto Basin analyzed in this study (refer to the section on structural data). The new AHe ages obtained in this study, being consistently younger than stratigraphic age of the sampled units (Tables 1 and 2), provide evidence for burial conditions sufficient to completely reset the AHe system that is in the range of 2.5–3.5 km (see below). Indeed, the presence of a few thousands of meters of burial is consistent with tectonic stylolite formation and folding of competent units of the Cañadón Asfalto succession (refer to Figures 5 and 6). Had such folding occurred during the Miocene, the removal of the overlying burial would be recorded by recent (i.e., Miocene or younger) AHe ages. Yet AHe ages obtained in this study point to a Late Cretaceous to Paleogene major tectonic inversion and exhumation stage, in agreement with a regional shortening stage that has been documented for the whole Patagonian Andes and its foreland, which lasted from circa 125 Ma to circa 56 Ma at the latitudes of this study [*Gianni et al*., 2015b]. The plate-scale extent of this major shortening stage is testified by fault reactivation and mild inversion occurring in Cretaceous times over various parts of the foreland area, as far as the Atlantic offshore [*Continanzia et al*., 2011; *Micucci et al*., 2011]. This suggests that the Cretaceous-Eocene inversion has been by far the dominant shortening event in the Gastre foreland sector and that the role and extent of Miocene inversion [e.g., *Bilmes et al*., 2013] are rather subordinate. The reduced role of Miocene inversion is in good agreement with a recent study by *Gianni et al*. [2015b], who suggested that the latest stages of Andean deformation and broken foreland reactivation during the Neogene (19.0–14.8 Ma) proposed by *Bilmes et al*. [2013] may have not been as strong as the Cretaceous-Paleogene event. Moreover, slightly tilted and locally gently folded 21.0 to 16.1 Ma old Miocene sediments documented by *Bilmes et al*. [2013] are unconformable with respect to intensely shortened Cañadón Asfalto strata that lower down in the succession, and the inferred reverse faults involving Miocene sediments drawn by the same authors in the Gastre area display vertical separations of a few hundreds of meters at most. Indeed, normal faulting appears to have mostly controlled the development of the various depocenters—including Miocene ones—in the Gastre area, whose structure has been consistently interpreted by *von Gosen and Loske* [2004] as "the result of (several stages of) downfaulting of different blocks that led to the formation of distinct young basins." On the other hand, preserved Late Cretaceous apatite fission track ages in the northern Patagonian Andes [*Thomson et al*., 2010] (Figure 3a) confirm that the regional Cretaceous-Paleogene shortening stage produced exhumation over the entire thrust belt-foreland system at these latitudes, despite being partially obliterated by Neogene rejuvenation of thrusting and unroofing in the frontal part of the thrust belt sector of the study area.

The AHe ages obtained from the thrust belt sector of the study area, ranging from 8.2 ± 0.9 Ma to 2.4 ± 0.2 Ma, are consistent with the regional Neogene exhumation event described by *Folguera and Ramos* [2011]. AHe ages are generally younger than apatite fission track ages available for the study area (Figures 3a and 3b), thus

being fully consistent with published thermochronological results. These two thermochronological methods provide information related to depths from 2.5 to 5 km, assuming geothermal gradient values of 20–25° C km^{-1} [*Jordan et al*., 1989; *Coughlin et al*., 1998; *Carrapa et al*., 2008; *Collo et al*., 2011; *Dávila and Carter*, 2013] and well-established closure temperatures for the two systems [*Ketcham*, 1999; *Gautheron et al*., 2009; *Flowers et al*., 2009; *Djimbi et al*., 2015]. Therefore, our data provide an effective record of the previously unconstrained final stages of exhumation in the study area. The integration of our AHe data with published apatite fission track ages indicates that, in the thrust belt sector of the study area, exhumation from 4.5 to 6.0 km depths started mainly during the Middle Miocene and continued through the uppermost 2.5–3.5 km of the crust mostly in Late Miocene to Pliocene times. Exhumation rates can be roughly estimated at 0.3 km/Myr for the Middle Miocene and then they raised at about 1.5 km/Myr. The recorded exhumation in the frontal part of the east vergent orogen correlates well with the Neogene shortening event well documented for this area [*Ramos et al*., 2011; *Folguera and Ramos*, 2011; *Orts et al*., 2012, 2015; *Echaurren et al*., 2016]. Taking into account the relatively simple tectonic setting of the outer Patagonian Andes and the lack of major structures (e.g., low-angle extensional detachments) that could control exhumation, this process is best interpreted as a result of thrust-related rock uplift and coeval erosion (that is known to have occurred at a rate of ~1 km/Myr since the Late Miocene at 41–42°S) [*Glodny et al*., 2006, and references therein]. Therefore, AHe ages are likely to record reverse fault activity—and related hanging wall uplift—in the study area. If this is the case, the exhumation pattern revealed by the projected cooling ages onto the cross sections of Figure 3b points to a lack of systematic sequential propagation of the deformation in the frontal part of the thrust belt. This is consistent with the thick-skinned tectonic inversion style of deformation widely documented for the Patagonian Andes [e.g., *Folguera and Ramos*, 2011; *Orts et al*., 2012, 2015]. By such style of crustal shortening, reverse faulting is controlled by the reactivation of inherited structures rather than progressively younger thrust propagation in the footwall of previously developed thrusts. Therefore, within the general framework of eastward growth of the Andean fold and thrust belt documented by the analysis of synorogenic sediments [*Ramos et al*., 2011; *Morabito and Ramos*, 2012; *Orts et al*., 2012; *Echaurren et al*., 2016], individual fault activity and related block uplift are likely to vary irregularly both in space and time. The complex interactions between local block uplift and erosion may result in an irregular unroofing pattern such as that shown in Figure 3a, which, however, is bracketed in time by the overall duration of a bulk regional shortening event (of Middle Miocene to Pliocene age in our instance).

Exhumation in the thrust belt sector of the study area appears to be related with an eastward migration of the magmatic arc between 15 and 11 Ma, marked by a series of satellite magmatic bodies throughout the eastern Andean side; this was accompanied by enlargement and deepening of the foreland basin, associated with the highest shortening rates recorded for this segment of the Patagonian Andes [*Orts et al*., 2015]. More to the south, between 45° and 48°S, *Guillaume et al*. [2013] interpreted a Miocene-Pliocene acceleration of exhumation, also unraveled by *Thomson et al*. [2001], as driven by mantle flow associated with slab window opening. There, the shortening stage started at around 32 Ma and ceased at 16–14 Ma [*Lagabrielle et al*., 2004]. During this period, close to the Chile Triple Junction, the South Chile Ridge did not enter the subduction zone and exhumation was only linked to the approach of the ridge close to the subduction zone [*Lagabrielle et al*., 2004]. At 16–14 Ma, ridge subduction started south of 52°S and opening of a slab window marked the end of the shortening event. At the Chile Triple Junction, a slab window developed at around 5–3 Ma, inducing extensional deformation [*Scalabrino et al*., 2010, 2011] and probably thermal doming-linked exhumation. On the other hand, a different explanation for Pliocene exhumation recorded more to the north (around 30°S) was provided by *Fosdick et al*. [2015], who related exhumation to out-of-sequence thrusting produced by a change in stress regime during Pampean flat-slab subduction.

The variability of deformation along the strike of the Andes has been related to the alternation of flat and steep slab segments [e.g., *Jordan et al*., 1983]. For the Central Andes, a large number of studies analyzed the sedimentary, magmatic, and structural evidence of past changes in the subduction configuration [e.g., *Allmendinger et al*., 1997; *Orts et al*., 2015, and references therein]. Orogeny in mid-Cretaceous times affected most of the South American margin, possibly being controlled by an acceleration of the continent motion during its westward drifting [*Somoza and Zaffarana*, 2008]. However, recently, *Gianni et al*. [2015b], using *Maloney et al*. [2013] data to reconstruct the average trench normal convergence and absolute velocity of the South American plate from 140 Ma to the present, pointed out close spatial and temporal relations among deformation of the broken foreland sector, development of the Chubut Group Basin, magmatic arc

migration, and a series of mid-ocean ridge collisions. All of these processes appear to have converged to enhance orogeny, as indicated by the synorogenic sedimentation described by *Gianni et al*. [2015b], with regional shortening being accompanied by vast—though discontinuously distributed—deformation over the whole South American plate from the Andes to the offshore area of the Atlantic passive margin [*Gianni et al*., 2015b].

The onset of shortening at around 100 Ma coincided with the change in absolute motion of South America related to the final breakup of western Gondwana [*Ramos*, 2010]. In late Eocene to early Miocene, trench normal absolute velocity of the South American plate remained particularly low [*Maloney et al*., 2013]. However, plate convergence increased again at 23 Ma (above 4 cm/a), with a peak of 6 cm/yr from ~20 to 15 Ma [*Pardo-Casas and Molnar*, 1987; *Maloney et al*., 2013]. This peak velocity is coincident with the latest stages of Andean shortening, triggering exhumation in the thrust belt sector of our study area (Figure 3), where final cooling through the ~65°C isotherm reaches the Pliocene (Table 2). On the other hand, the Neogene broken foreland reactivation at 19.0–14.8 Ma [*Bilmes et al*., 2013] occurred in a period characterized by no general arc expansion [*Gianni et al*., 2015b, and references therein]. This rules out the possibility of a long-standing flat-slab segment during this time span, as already pointed out by *Bilmes et al*. [2013] themselves. As a matter of fact, our new low-T thermochronometric data provide no evidence for major reverse-slip fault reactivation and tectonic inversion in the Gastre foreland sector at kilometric scale during the Neogene, despite the fact that the closure temperature of the apatite (U-Th)/He system makes the applied geochronological method as the most appropriate to unravel exhumation throughout the uppermost part of the crust. Therefore, Miocene tectonic inversion in the Gastre area must have been very mild and limited, and it did not produce any significant exhumation.

In synthesis, our results suggest that, during periods of steep-slab subduction and rollback, high convergence rates (above 4 cm/yr) [*Maloney et al*., 2013] are able to produce shortening in the fold and thrust belt, but far-field stress propagation and tectonic inversion in the foreland are relatively minor, the foreland being essentially uncoupled from the thrust belt (Figure 9a). On the other hand, a flat-slab configuration, probably associated with thermal weakening of the overriding plate imposed by prolonged mid-ocean ridge subduction [*Martinod et al*., 2005; *Ramos*, 2005], leads to regional shortening involving both the thrust belt and the foreland (Figure 9b). This is consistent with geological observations and insights from analog modeling, which suggest that the occurrence of horizontal slab segments results in stronger interplate coupling [*Martinod et al*., 2010]. This, besides relatively high shortening rates in the orogen [*Guillaume et al*., 2009], also produces widespread shortening of continental plate interiors [*Martinod et al*., 2010]. During these stages of flat-slab subduction, the foreland sector may therefore experience tectonic inversion triggering substantial exhumation. This coupling of the deformation may be effective even at very large distances (i.e., many hundreds of kilometers) from the subduction trench, as it occurred during Late Cretaceous to Paleogene times in the Patagonian Andes.

6. Conclusions

Our study suggests that configurations of flat-slab versus steep-slab subduction may exert an important role in controlling the coupling versus uncoupling of the deformation between the thrust belt and its foreland in the Patagonian Andes. Of course, the complexity of the structural architecture of this vast area implies that deformation is heterogeneously distributed in both space and time. Within this framework, the simple model depicted in the cartoon of Figure 9 is intended to represent just a general rule of thumb. As recently pointed out by *Gianni et al*. [2015b], throughout the Andean evolution of the Patagonian foreland, extensional basins have acted as anisotropies effectively focalizing strain during shortening. This process led to a localized tectonic inversion of foreland sectors as far as the distal broken foreland of the Atlantic offshore. These shortened sectors are separated by relatively undeformed areas. Such a heterogeneous style of upper plate deformation during Andean orogenesis had been reported previously at a continental scale for the whole South American plate [*Cobbold et al*., 2007]. The results of this study confirm the complexity and relevance of foreland deformation, probably beyond the simple notion of propagation of horizontal compression into the foreland area during the main stages Andean orogenesis. In particular, the spatial distribution of tectonic inversion and associated exhumation, being focused in the thrust belt or spreading over wide foreland sectors as well, appears to be controlled by deep geodynamic processes (i.e., slab rollback versus flat-slab

subduction). Late Miocene to Pliocene AHe ages from the frontal part of the northern Patagonian Andes correlate well with a shortening and exhumation stage documented to have occurred in the thrust belt during steep subduction characterized by high convergence rates (>4 cm/a). On the other hand, AHe ages obtained for the first time in this study for the broken foreland unraveled final exhumation at near-surface conditions (i.e., through the ~100–50°C HePRZ) during Late Cretaceous to Paleogene times. This is envisaged to have occurred by the upward extrusion of the sedimentary fills of Mesozoic grabens/half-grabens, accompanied by folding of the sedimentary successions caught between rigid basement blocks, and by substantial unroofing produced by erosion of the overlying uplifted sedimentary cover. This process was coeval with a major shortening stage in the thrust belt, associated with a period of flat-slab subduction. Coupling of the deformation during such a period was probably enhanced by thermal weakening of the overriding plate as a result of mid-ocean ridge subduction [*Ramos*, 2005], resulting in plate-scale heterogeneous shortening.

Acknowledgments

Thoughtful and constructive reviews by Bruno Scalabrino and an Anonymous Referee and the useful comments by Associate Editor M. Jolivet and Editor C. Faccenna are thankfully acknowledged. Funding for this work was provided by the University of Padova (Progetto di Ateneo 2015, CPDA158355) to E. Savignano and M. Zattin; the University of Naples Federico II (Fondi Ricerca Dipartimentale) to S. Mazzoli; and the Universidad Nacional de Río Negro (PICT-FONCyT 2013-2916, PIP-CONICET 330, U.N. Comahue) to M. Arce and M. Franchini. We are grateful to Pan American Silver for the precious collaboration and fruitful discussion of data and for allowing the survey activity in the Navidad area. S. Boesso, R. Pinna, and L. Bordier are thanked for AHe sample preparation, analysis of U-Th chemistry, and for assisting during ICP-MS measurements at LSCE (Gif-sur-Yvette). E. Douville is thanked for providing access to the ICP-MS system. Move software, for which Midland Valley Ltd. is gratefully acknowledged, was used both in the field (Field Clino) and in the lab (academic licenses available at the University of Padova and the University of Naples Federico II).

References

Allard, J. O., R. Giacosa, and J. Paredes (2011), Relaciones estratigráficas entre la Formación Los Adobes (Cretácico Inferior) y su sustrato Jurásico: Implicancias en la evolución tectónica de la cuenca de Cañadón Asfalto, Chubut, Argentina, paper presented at VIII Congreso Geológico Argentino, Neuquén, Argentina.

Allmendinger, R. W., T. E. Jordan, S. M. Kay, and B. L. Isacks (1997), The evolution of the Altiplano-Puna plateau of the central Andes, *Annu. Rev. Earth Planet. Sci.*, *25*, 139–174.

Allmendinger, R. W., N. C. Cardozo, and D. Fisher (2012), *Structural Geology Algorithms: Vectors & Tensors*, pp. 289, Cambridge Univ. Press, Cambridge, U. K.

Angelier, J., and P. Mechler (1977), Sur une méthode graphique de recherche des contraintes principales égalementutilisable en tectonique et en séismologie: La méthode des dièdres droits, *Bull. Soc. Geol. Fr.*, *19*, 1309–1318.

Aragón, E., et al. (2011), Tectono-magmatic response to major convergence changes in the North Patagonian suprasubduction system: The Paleogene subduction–transcurrent plate margin transition, *Tectonophysics*, *509*(3).

Ardolino, A. A., F. M. Salani, and A. Lizuaín (2009), Hoja 4166–III, Gan Gan. Escala 1: 250.000, Provincia del Chubut, modificado 2005: Instituto de Geología y Recursos Minerales, Servicio Geológico Minero Argentino, 1-200.

Bechis, F., and E. O. Cristallini (2006), Inflexiones en estructuras del sector norte de la faja plegada y corrida de Ñirihuau, provincia de Río Negro, *Rev. Asoc. Geol. Argentina, Publ. Espec.*, *6*, 18–25.

Bechis, F., A. Encinas, A. Concheyro, V. D. Litvak, B. Aguirre-Urreta, and V. A. Ramos (2014), New age constraints for the Cenozoic marine transgressions of northwestern Patagonia, Argentina (41–43 S): Paleogeographic and tectonic implications, *J. South Am. Earth Sci.*, *52*, 72–93.

Bellahsen, N., L. Jolivet, O. Lacombe, M. Bellanger, A. Boutoux, S. Garcia, F. Mouthereau, L. Le Pourhiet, and C. Gumiaux (2012), Mechanisms of margin inversion in the external Western Alps: Implications for crustal rheology, *Tectonophysics*, *560*, 62–83.

Bilmes, A. (2012), Caracterización estratigráfica, sedimentológica y estructural del sistema de bajos neógenos de Gastre, provincias de Río Negro y de Chubut, PhD thesis, Facultad de Ciencias Naturales y Museo, Universidad Nacional de La Plata, La Plata.

Bilmes, A., L. D'Elia, J. R. Franzese, G. D. Veiga, and M. Hernández (2013), Miocene block uplift and basin formation in the Patagonian foreland: The Gastre Basin, Argentina, *Tectonophysics*, *601*, 98–111.

Bott, M. H. P. (1959), The mechanics of oblique slip faulting, *Geol. Mag.*, *96*, 109–117.

Butler, R. W., and S. Mazzoli (2006), Styles of continental contraction: A review and introduction, *Geol. Soc. Am. Spec. Pap.*, *414*, 1–10.

Cardozo, N., and R. W. Allmendinger (2013), Spherical projections with OSXStereonet, *Comput. Geosci.*, *51*, 193–205.

Carrapa, B., J. Hauer, L. Schoenbohm, M. R. Strecker, A. K. Schmitt, A. Villanueva, and J. Sosa Gomez (2008), Dynamics of deformation and sedimentation in the northern Sierras Pampeanas: An integrated study of the Neogene Fiambalá basin, NW Argentina, *Geol. Soc. Am. Bull.*, *120*, 1518–1543.

Castro, A., et al. (2011), Petrology and SHRIMP U–Pb zircon geochronology of Cordilleran granitoids of the Bariloche area, Argentina, *J. South Am. Earth Sci.*, *32*(4), 508–530.

Cazau, L., D. Mancini, J. Cangini, and L. Spalletti (1989), Cuenca de Ñirihuau, in *Cuencas Sedimentarias Argentinas*, vol. 6, edited by G. Chebli and L. Sapalletti, pp. 299–318, Serie Correlación Geológica, Tucumán, Argentina.

Cembrano, J., F. Hervé, and A. Lavenu (1996), The Liquiñe Ofqui fault zone: A long-lived intra-arc fault system in southern Chile, *Tectonophysics*, *259*(1), 55–66.

Charrier, R., O. Baeza, S. Elgueta, J. Flynn, P. Gans, S. M. Kay, N. Muñoz, A. R. Wyss, and E. Zurita (2002), Evidence for Cenozoic extensional basin development and tectonic inversion south of the flat-slab segment, southern Central Andes, Chile (33–36 SL), *J. South Am. Earth Sci.*, *15*(1), 117–139.

Cobbold, P. R., E. A. Rossello, P. Roperch, C. Arriagada, L. A. Gómez, and C. Lima (2007), Distribution, timing, and causes of Andean deformation across South America, *Geol. Soc. London Spec. Publ.*, *272*(1), 321–343.

Coira, B., F. Nullo, C. Proserpio, and V. A. Ramos (1975), Tectónica de basamento de la región occidental del Macizo Nordpatagónico (Provincias de Río Negro y Chubut), República Argentina, *Rev. Asoc. Geol. Argent.*, *30*(4), 361–383.

Collo, G., F. M. Dávila, J. Nóbile, R. A. Astini, and G. Gehrels (2011), Clay mineralogy and thermal history of the Neogene Vinchina Basin, central Andes of Argentina: Analysis of factors controlling the heating conditions, *Tectonics*, *30*, TC4012, doi:10.1029/2010TC002841.

Continanzia, J., R. Manceda, G. M. Covellone, and A. S. Gavarrino (2011), Cuencas de Rawson y Valdés: Síntesis del Conocimiento Exploratorio—Visión actual, in *VIII Congreso de Exploración y Desarrollo de Hidrocarburos*, edited by E. Kozlowski, pp. 47–64, Simposio Cuencas Argentinas Visión Actual, Mar de La Plata, Buenos Aires.

Coughlin, T. J., P. B. O'Sullivan, P. B. Kohn, and R. J. Holcombe (1998), Apatite fission-track termochronology of the Sierras Pampeanas, central western Argentina: Implications for the mechanism of plateau uplift in the Andes, *Geology*, *26*, 999–1002.

Coward, M. P. (1994), Continental collision, in *Continental Deformation*, edited by P. L. Hancock, pp. 264–288, Pergamon, New York.

Cúneo, R., J. Ramezani, R. Scasso, D. Pol, I. Escapa, A. M. Zavattieri, and S. A. Bowring (2013), High-precision U–Pb geochronology and a new chronostratigraphy for the Cañadón Asfalto Basin, Chubut, central Patagonia: Implications for terrestrial faunal and floral evolution in Jurassic, *Gondwana Res.*, *24*(3), 1267–1275.

Dalla Salda, L., and J. Franzese (1987), Las megaestructuras del Macizo y Cordillera Norpatagónica Argentina y la génesis de las cuencas volcanosedimentarias Terciarias, *Rev. Geol. Chile*, *31*, 3–13.
Dávila, F. M., and A. Carter (2013), Exhumation history of the Andean broken foreland revisited, *Geology*, *41*(4), 443–446.
DeMets, C., R. G. Gordon, D. F. Argus, and S. Stein (1990), Current plate motions, *Geophys. J. Int.*, *101*(2), 425–478.
Djimbi, D. M., C. Gautheron, J. Roques, L. Tassan-Got, C. Gerin, and E. Simoni (2015), Impact of apatite chemical composition on (U-Th)/He thermochronometry: An atomistic point of view, *Geochim. Cosmochim. Acta*, *167*, 162–176.
Duhart, P., M. Haller, and F. Hervé (2002), Diamictitas como parte del protolito de las metamorfitas de la Formación Cushamen en Río Chico, provincias de Río Negro y Chubut, Argentina, in: *XV Congreso Geológico Argentino*, *Actas*, *2*, 97–100, El Calafate.
Echaurren, A., A. Folguera, G. Gianni, D. Orts, A. Tassara, A. Encinas, M. Giménez, and V. Valencia (2016), Tectonic evolution of the North Patagonian Andes (41°–44°S) through recognition of syntectonic strata, *Tectonophysics*, *677*, 99–114.
Encinas, A., K. L. Finger, L. A. Buatois, and D. E. Peterson (2012), Major forearc subsidence and deep-marine Miocene sedimentation in the present Coastal Cordillera and Longitudinal Depression of south-central Chile (38°30′S–41°45′S), *Geol. Soc. Am. Bull.*, *124*(7–8), 1262–1277.
Fillon, C., C. Gautheron, and P. A. van der Beek (2013), Oligocene-Miocene burial and exhumation of the Southern Pyrenean foreland quantified by low-temperature thermochronology, *J. Geol. Soc.*, *170*, 67–77.
Flowers, R. M., R. A. Ketcham, D. L. Shusterand, and K. A. Farley (2009), Apatite (U–Th)/He thermochronometry using a radiation damage accumulation and annealing model, *Geochim. Cosmochim. Acta*, *73*(8), 2347–2365.
Folguera, A., and V. A. Ramos (2011), Repeated eastward shifts of arc magmatism in the Southern Andes: A revision to the long-term pattern of Andean uplift and magmatism, *J. S. Am. Earth Sci.*, *32*(4), 531–546.
Folguera, A., G. Bottesi, I. Duddy, F. Martín-González, D. Orts, L. Sagripanti, E. Rojas Vera, and V. A. Ramos (2015), Exhumation of the Neuquén Basin in the southern Central Andes (Malargüe fold and thrust belt) from field data and low-temperature thermochronology, *J. S. Am. Earth Sci.*, *64*, 381–398.
Fosdick, J. C., B. Carrapa, and G. Ortíz (2015), Faulting and erosion in the Argentine Precordillera during changes in subduction regime: Reconciling bedrock cooling and detrital records, *Earth Planet. Sci. Lett.*, *432*, 73–83.
Gautheron, C., and L. Tassan-Got (2010), A Monte Carlo approach to diffusion applied to noble gas/helium thermochronology, *Chem. Geol.*, *273*(3), 212–224.
Gautheron, C., L. Tassan-Got, J. Barbarand, and M. Pagel (2009), Effect of alpha-damage annealing on apatite (U–Th)/He thermochronology, *Chem. Geol.*, *266*(3), 157–170.
Gautheron, C., L. Tassan-Got, R. A. Ketchamand, and K. J. Dobson (2012), Accounting for long alpha-particle stopping distances in (U–Th–Sm)/He geochronology: 3D modeling of diffusion, zoning, implantation, and abrasion, *Geochim. Cosmochim. Acta*, *96*, 44–56.
Geiser, P., and T. Engelder (1983), The distribution of layer parallel shortening fabrics in the Appalachian foreland of New York and 'Pennsylvania: Evidence for two non-coaxial phases of the Alleghanian orogeny, *Geol. Soc. Am. Mem.*, *158*, 161–176.
Giacosa, R. E., and N. Heredia (2004a), Estructura de los Andes Nordpatagónicos en los cordones Piltriquitrón y Serrucho y en el valle de El Bolsón (41°30′–42°00′S), Río Negro, *Rev. Asoc. Geol. Argent.*, *59*(1), 91–102.
Giacosa, R. E., and N. Heredia (2004b), Structure of the North Patagonian thick-skinned fold-and-thrust belt, southern central Andes, Argentina (41–42 S), *J. S. Am. Earth Sci.*, *18*(1), 61–72.
Giacosa, R. E., J. C. Afonso, N. Heredia, and J. Paredes (2005), Tertiary tectonics of the sub-Andean region of the North Patagonian Andes, southern central Andes of Argentina (41–42°30′S), *J. S. Am. Earth Sci.*, *20*(3), 157–170.
Gianni, G. M., C. G. Navarrete, and A. Folguera (2015b), Synorogenic foreland rifts and transtensional basins: A review of Andean imprints on the evolution of the San Jorge Gulf, Salta Group and Taubaté Basins, *J. S. Am. Earth Sci.*, *64*, 288–306.
Gianni, G., C. Navarrete, D. Orts, J. Tobal, A. Folguera, and M. Giménez (2015a), Patagonian broken foreland and related synorogenic rifting: The origin of the Chubut Group Basin, *Tectonophysics*, *649*, 81–99.
Glodny, J., et al. (2006), Long-term geological evolution and mass-flow balance of the South-Central Andes, in *The Andes*, pp. 401–428, Springer, Berlin Heidelberg.
Godoy, E., G. Yáñez, and E. Vera (1999), Inversion of an Oligocene volcano-tectonic basin and uplifting of its superimposed Miocene magmatic arc in the Chilean Central Andes: First seismic and gravity evidences, *Tectonophysics*, *306*(2), 217–236.
González, E. (1989), Hydrocarbon resources in the coastal zone of Chile, in *Geology of the Andes and Its Relation to Hydrocarbon and Mineral Resources*, edited by J. A. Reinemund, G. E. Ericksen, and M. T. Cañas Pinochet, pp. 383–404, Circum-Pacific Council for Energy and Mineral Resources, Houston, TX.
Gordon, A., and M. H. Ort (1993), Edad y correlación del plutonismo subcordillerano en las provincias de Río Negro y Chubut (41–42°30′LS), *Congreso Geol. Argent.*, *12*, 120–127.
Gripp, A. E., and R. G. Gordon (1990), Current plate velocities relative to the hotspots incorporating the NUVEL-1 global plate motion model, *Geophys. Res. Lett.*, *17*(8), 1109–1112, doi:10.1029/GL017i008p01109.
Guillaume, B., J. Martinod, and N. Espurt (2009), Variations of slab dip and overriding plate tectonics during subduction: Insights from analogue modeling, *Tectonophysics*, *463*, 167–174.
Guillaume, B., C. Gautheron, T. Simon-Labric, J. Martinod, M. Roddaz, and E. Douville (2013), Dynamic topography control on Patagonian relief evolution as inferred from low temperature thermochronology, *Earth Planet. Sci. Lett.*, *364*, 157–167.
Gutscher, M. A. (2002), Andean subduction styles and their effect on thermal structure and interplate coupling, *J. South Am. Earth Sci.*, *15*(1), 3–10.
Haschke, M. R., E. Scheuber, A. Günther, and K. J. Reutter (2002), Evolutionary cycles during the Andean orogeny: Repeated slab breakoff and flat subduction? *Terra Nova*, *14*(1), 49–55.
Hervé, F. (1994), The southern Andes between 39 and 44 S latitude: The geological signature of a transpressive tectonic regime related to a magmatic arc, in *Tectonics of the Southern Central Andes*, pp. 243–248, Springer, Berlin Heidelberg.
Holdsworth, R. E., M. Handa, J. A. Miller, and I. S. Buick (2001), Continental reactivation and reworking: An introduction, *Geol. Soc. London Spec. Publ.*, *184*(1), 1–12.
Homovc, J. F., C. Navarrete, P. Marshall, S. Masquere, and J. Cerdan (2011), Inversión tectónica intra-cretácica de la Subcuenca de Río Mayo, Chubut, Argentina, in: *XVIII Congreso Geológico Argentino*, 1418–1419.
Humphreys, E. (2009), Relation of flat subduction to magmatism and deformation in the western United States, *Geol. Soc. Am. Mem.*, *204*, 85–98.
Jordan, T. E., B. Isacks, V. A. Ramos, and R. W. Allmendinger (1983), Mountain building in the Central Andes, *Episodes*, *3*, 20–26.
Jordan, T. E., P. Zeitler, V. A. Ramos, and A. J. W. Gleadow (1989), Thermochronometric data on the development of the basement peneplain in the Sierras Pampeanas, Argentina, *J. S. Am. Earth Sci.*, *2*, 207–222.
Jordan, T. E., W. M. Burns, R. Veiga, F. Pángaro, P. Copeland, S. Kelley, and C. Mpodozis (2001), Extension and basin formation in the southern Andes caused by increased convergence rate: A mid-Cenozoic trigger for the Andes, *Tectonics*, *20*(3), 308–324, doi:10.1029/1999TC001181.

Kay, S. M., and B. L. Coira (2009), Shallowing and steepening subduction zones, continental lithospheric loss, magmatism, and crustal flow under the Central Andean Altiplano-Puna Plateau, *Geol. Soc. Am. Mem.*, *204*, 229–259.
Kendrick, E. C., M. Bevis, R. F. Smalley Jr., O. Cifuentes, and F. Galban (1999), Current rates of convergence across the Central Andes: Estimates from continuous GPS observations, *Geophys. Res. Lett.*, *26*(5), 541–544, doi:10.1029/1999GL900040.
Ketcham, R. A. (2005), Forward and inverse modeling of low-temperature thermochronometry data, *Rev. Mineral. Geochem.*, *58*(1), 275–314.
Ketcham, R. A., C. Gautheron, and L. Tassan-Got (2011), Accounting for long alpha-particle stopping distances in (U–Th–Sm)/He geochronology: Refinement of the baseline case, *Geochim. Cosmochim. Acta*, *75*(24), 7779–7791.
Kley, J., C. R. Monaldi, and J. A. Salfity (1999), Along-strike segmentation of the Andean foreland: Causes and consequences, *Tectonophysics*, *301*(1), 75–94.
Kraml, M., R. Pik, M. Rahn, R. Selbekk, J. Carignan, and J. Keller (2006), A new multi-mineral age reference material for $^{40}Ar/^{39}Ar$,(U-Th)/He and fission track dating methods: The Limberg t3 Tuff, *Geostand. Geoanal. Res.*, *30*(2), 73–86.
Lacombe, O., and F. Mouthereau (2002), Basement-involved shortening and deep detachment tectonics in forelands of orogens: Insights from recent collision belts (Taiwan, Western Alps, Pyrenees), *Tectonics*, *21*(4), 1030, doi:10.1029/2001TC901018.
Lagabrielle, Y., M. Suárez, E. A. Rossello, G. Hérail, J. Martinod, M. Régnier, and R. de la Cruz (2004), Neogene to Quaternary tectonic evolution of the Patagonian Andes at the latitude of the Chile Triple Junction, *Tectonophysics*, *385*(1), 211–241.
Lavenu, A., and J. Cembrano (1999), Compressional-and transpressional-stress pattern for Pliocene and Quaternary brittle deformation in fore arc and intra-arc zones (Andes of Central and Southern Chile), *J. Struct. Geol.*, *21*(12), 1669–1691.
Lesta, P., and R. Ferello (1972), Región extraandina de Chubut y norte de Santa Cruz, *Geol. Reg. Argent.*, *2*, 602–687.
Lizuaín, A. (2009), Hoja 4372–II, Esquel. Escala 1: 250.000, Provincia del Chubut: Instituto de Geología y Recursos Minerales, Servicio Geológico Minero Argentino.
Lizuaín, A., and D. Silva Nieto (2011), Hoja 4369-I, Gastre. Escala 1: 250.000, Provincia del Chubut: Instituto de Geología y Recursos Minerales, Servicio Geológico Minero Argentino.
Maloney, K. T., G. L. Clarke, K. A. Klepeis, and L. Quevedo (2013), The Late Jurassic to present evolution of the Andean margin: Drivers and the geological record, *Tectonics*, *32*, 1049–1065, doi:10.1002/tect.20067.
Mancini, D., and M. Serna (1989), Evaluación petrolera de la Cuenca de Ñirihuau. Sudoeste de Argentina, in *1th Congreso Nacional de Exploración de Hidrocarburos (Argentina)*, pp. 739–762, Inst. Argent. del Petról., Buenos Aires.
Marrett, R. A., and R. W. Allmendinger (1990), Kinematic analysis of fault-slip data, *J. Struct. Geol.*, *12*, 973–986.
Martinod, J., F. Funiciello, C. Faccenna, S. Labanieh, and V. Regard (2005), Dynamical effects of subducting ridges: Insights from 3-D laboratory models, *Geophys. J. Int.*, *163*, 1137–1150.
Martinod, J., L. Husson, P. Roperch, B. Guillaume, and N. Espurt (2010), Horizontal subduction zones, convergence velocity and the building of the Andes, *Earth Planet. Sci. Lett.*, *299*(3), 299–309.
Massaferro, G. I., M. J. Haller, M. D'Orazio, and V. I. Alric (2006), Sub-recent volcanism in Northern Patagonia: A tectonomagmatic approach, *J. Volcanol. Geotherm. Res.*, *155*(3), 227–243.
Mazzoli, S., S. Vitale, G. Delmonaco, V. Guerriero, C. Margottini, and D. Spizzichino (2009), 'Diffuse faulting' in the Macchu Picchu granitoid pluton, Eastern Cordillera, Peru, *J. Struct. Geol.*, *31*, 1395–1408.
Mazzoni, M. M., K. Kawashita, S. Harrison, and E. Aragón (1991), Edades radimetricas eocenas, Borde occidental del Macizo Norpatagonico, *Asoc. Geol. Argent. Rev.*, *46*(1–2), 150–158.
McDowell, F. W., W. C. McIntosh, and K. A. Farley (2005), A precise $^{40}Ar–^{39}Ar$ reference age for the Durango apatite (U–Th)/He and fission-track dating standard, *Chem. Geol.*, *214*(3), 249–263.
Mescua, J. F., L. Giambiagi, and F. Bechis (2012), Reply to L.V. Dimieri and M.M. Turienzo, 2012 comment on: "Fault inversion vs. new thrust generation: A case study in the Malargüe fold-and thrust belt, Andes of Argentina" by J. F. Mescua and, L. B. Giambiagi, *J. Struct. Geol.*,35 (2012) 51–63, *J. Struct. Geol.*, *42*, 283–287.
Micucci, E. M., J. Continanzia, R. Manceda, and A. S. Gavarrino (2011), Cuenca de San Julián: Síntesis del conocimiento exploratorio—Visión actual, in *VIII Congreso de Exploración y Desarrollo de Hidrocarburos*, edited by E. Kozlowski, Simposio Cuencas Argentinas Visión Actual,17-4, Mar de La Plata, Buenos Aires.
Morabito, E. G., and V. A. Ramos (2012), Andean evolution of the Aluminé fold and thrust belt, Northern Patagonian Andes (38°30′–40°30′S), *J. S. Am. Earth Sci.*, *38*, 13–30.
Orts, D. L., A. Folguera, A. Encinas, M. Ramos, J. Tobal, and V. A. Ramos (2012), Tectonic development of the North Patagonian Andes and their related Miocene foreland basin (41°30′–43°S), *Tectonics*, *31*, TC3012, doi:10.1029/2011TC003084.
Orts, D. L., A. Folguera, M. Giménez, F. Ruiz, E. A. R. Vera, and F. L. Klinger (2015), Cenozoic building and deformational processes in the North Patagonian Andes, *J. Geodyn.*, *86*, 26–41.
Pankhurst, R. J., S. D. Weaver, F. Hervé, and P. Larrondo (1999), Mesozoic-Cenozoic evolution of the North Patagonian batholith in Aysén, southern Chile, *J. Geol. Soc.*, *156*(4), 673–694.
Pankhurst, R. J., C. W. Rapela, C. M. Fanning, and M. Márquez (2006), Gondwanide continental collision and the origin of Patagonia, *Earth Sci. Rev.*, *76*(3), 235–257.
Pardo-Casas, F., and P. Molnar (1987), Relative motion of the Nazca (Farallon) and South American plates since Late Cretaceous time, *Tectonics*, *6*(3), 233–248, doi:10.1029/TC006i003p00233.
Pfiffner, O. A., and M. Burkhard (1987), Determination of paleo-stress axes orientations from fault, twin and earthquake data, *An. Tec.*, *1*(1), 48–57.
Proserpio, C. A. (1978), Descripción geológica de la Hoja 42d, Gastre, Provincia del Chubut: Carta geológica-económica de la República Argentina, escala 1: 200.000. Servicio Geológico Nacional.
Radic, J. P., L. Rojas, A. Carpinelli, and E. Zurita (2002), Evolucion tectonica de la Cuenca terciaria de Cura Mallín, region cordillerana chileno argentina (36300e39000S), in: *XV Congreso Geologico Argentino*, *Actas*, *3*, 233–237, Calafate.
Radic, J. P., P. Alvarez, L. Rojas, C. Czollak, R. Parada, and V. Ortiz (2009), La cuenca de Val-divia como parte del sistema de antearco de la plataforma continental de ChileCentral entre los 36°y los 40°S, in: *XII Congreso Geológico Chileno*, *Asociación Geológica de Chile*, Santiago, Chile, S10-032.
Ramos, M. E., D. L. Orts, F. Calatayud, P. J. Pazos, A. Folguera, and V. A. Ramos (2011), Estructura, estratigrafía y evolución tectónica de la cuenca de Nirihuau en las nacientes del río Cushamen, Chubut, *Rev. Asoc. Geol. Argent.*, *68*, 210–224.
Ramos, M. E., A. Folguera, L. Fennell, M. Giménez, V. D. Litvak, Y. Dzierma, and V. A. Ramos (2014), Tectonic evolution of the North Patagonian Andes from field and gravity data (39–40°S), *J. S. Am. Earth Sci*, *51*, 59–75.
Ramos, V. A. (1981), Descripción geológica de la hoja 47 ab Lago Fontana, Provincia de Chubut, *Serv. Geol. Nacional, Bol.*, *183*, 1–130.
Ramos, V. A. (1982), Las ingresiones pacíficas del Terciario en el norte de la Patagonia (Argentina), in: *IIICongreso Geológico Chileno*, *Actas*, A263-288, Conception.

Ramos, V. A. (2005), Seismic ridge subduction and topography: Foreland deformation in the Patagonian Andes, *Tectonophysics*, *399*, 73–86.
Ramos, V. A. (2010), The tectonic regime along the Andes: Present-day and Mesozoic regimes, *Geol. J.*, *45*(1), 2–25.
Ramos, V. A., and A. Folguera (2009), Andean flat-slab subduction through time, *Geol. Soc. London Spec. Publ.*, *327*(1), 31–54.
Ramos, V. A., and J. M. Cortés (1984), Estructura e interpretación tectónica, in *Geología y Recursos Naturales de la Provincia de Río Negro*, edited by V. A. Ramos, pp. 317–346, Asoc. Geol. Argent., Buenos Aires.
Ramsay, J. G., and M. I. Huber (1987), *The Techniques of Modern Structural Geology: Folds and Fractures*, vol. 2, Academic Press, London.
Rapela, C. W., L. A. Spalletti, J. C. Merodio, and E. Aragón (1988), Temporal evolution and spatial variation of early Tertiary volcanism in the Patagonian Andes (40°S–42°30′S), *J. S. Am. Earth Sci.*, *1*(1), 75–88.
Ravazzoli, I. A., and F. L. Sesana (1977), Descripción geológica de la Hoja 41c, Río Chico, *Serv. Geol. Nacional, Bol*, *148*, 77.
Reiners, P. W., and K. A. Farley (2001), Influence of crystal size on apatite (U–Th)/He thermochronology: An example from the Bighorn Mountains, Wyoming, *Earth Planet. Sci. Lett.*, *188*(3), 413–420.
Rosenau, M., D. Melnick, and H. Echtler (2006), Kinematic constraints on intra-arc shear and strain partitioning in the southern Andes between 38 S and 42 S latitude, *Tectonics*, *25*, TC4013, doi:10.1029/2005TC001943.
Scalabrino, B., Y. Lagabrielle, J. Malavieille, S. Dominguez, D. Melnick, F. Espinoza, M. Suarez, and E. Rossello (2010), A morphotectonic analysis of central Patagonian Cordillera: Negative inversion of the Andean belt over a buried spreading center?, *Tectonics*, *29*, TC2010, doi:10.1029/2009TC002453.
Scalabrino, B., J. F. Ritz, and Y. Lagabrielle (2011), Relief inversion triggered by subduction of an active spreading ridge: Evidence from glacial morphology in Central Patagonia, *Terra Nova*, *23*(2), 63–69.
Skármeta, J., and R. Charrier (1976), Geología del sector fronterizo de Aysén entre los 45 y 46 de latitud sur, Chile, in: *IV Congreso Geológico Argentino*, 267-286.
Somoza, R., and C. B. Zaffarana (2008), Mid-Cretaceous polar standstill of South America, motion of the Atlantic hotspots and the birth of the Andean cordillera, *Earth Planet. Sci. Lett.*, *271*(1), 267–277.
Spalletti, L. A., and L. H. Dalla Salda (1996), A pull apart volcanic related Tertiary basin, an example from the Patagonian Andes, *J. South Am. Earth Sci.*, *9*(3–4), 197–206.
Spalletti, L., J. Franzese, E. Morel, A. Zúñiga, and C. M. Fanning (2010), Consideraciones acerca de la sedimentología, paleobotánica y geocronología de la formación piedra del águila (jurásico inferior, Neuquén), *Rev. Asoc. Geol. Argent.*, *66*(3), 305–313.
Stern, C. R. (2004), Active Andean volcanism: Its geologic and tectonic setting, *Rev. Geol. Chile.*, *31*(2), 161–206.
Suárez, M., and R. de la Cruz (2001), Jurassic to Miocene K-Ar dates from eastern central Patagonian Cordillera plutons, Chile (45°–48°S), *Geol. Mag.*, *138*(1), 53–66.
Suárez, M., R. De La Cruz, and C. M. Bell (1996), Estratigrafía de la región de Coyhaique(Latitud 45°–46°S), Cordillera Patagónica, Chile, in: *XIII Congreso GeológicoArgentino and III Congreso de Exploración de Hidrocarburos*, 575–590.
Tavani, S., F. Storti, O. Lacombe, A. Corradetti, J. A. Muñoz, and S. Mazzoli (2015), A review of deformation pattern templates in foreland basin systems and fold-and-thrust belts: Implications for the state of stress in the frontal regions of thrust wedges, *Earth Sci. Rev.*, *141*, 82–104.
Thomson, S. N., and F. Hervé (2002), New time constraints for the age of metamorphism at the ancestral Pacific Gondwana margin of southern Chile (42–52 S), *Rev. Geol. Chile*, *29*(2), 255–271.
Thomson, S. N., F. Hervé, and B. Stöckhert (2001), Mesozoic-Cenozoic denudation history of the Patagonian Andes (southern Chile) and its correlation to different subduction processes, *Tectonics*, *20*(5), 693–711, doi:10.1029/2001TC900013.
Thomson, S. N., M. T. Brandon, J. H. Tomkin, P. W. Reiners, C. Vásquez, and N. J. Wilson (2010), Glaciation as a destructive and constructive control on mountain building, *Nature*, *467*(7313), 313–317.
Vargas Easton, G., S. Rebolledo, S. A. Sepúlveda, A. Lahsen, R. Thiele, B. Townley, C. Padilla, R. Rauld, M. J. Herrera, and M. Lara (2013), Submarine earthquake rupture, active faulting and volcanism along the major Liquiñe-Ofqui Fault Zone and implications for seismic hazard assessment in the Patagonian Andes, *Andean Geol.*, *40*(1), 141–171.
Volkheimer, W. (1964), Estratigrafía de la zona extraandina del Departamento de Cushamen (Chubut), *Rev. Asoc. Geol. Argent.*, *19*(2), 85–107.
von Gosen, W. (2009), Stages of Late Palaeozoic deformation and intrusive activity in the western part of the North Patagonian Massif (southern Argentina) and their geotectonic implications, *Geol. Mag.*, *146*(1), 48.
von Gosen, W., and W. Loske (2004), Tectonic history of Calcatapul Formation, Chubut Province, Argentina, and the "Gastre Fault System", *J. South Am. Earth Sci.*, *18*, 73–88.
Wallace, R. E. (1951), Geometry of shearing stress and relationship to faulting, *J. Geol.*, *59*, 111–130.
Williams, D. K. (2010), Geology and Mineralization of the Navidad Ag-Pb-Cu-Zn District, Chubut Province, Argentina, *Econ. Geol. Bull. Soc. Inc. Spec. Publ.*, *15*, 203–227.
Willner, A., J. Glodny, T. Gerya, E. Godoy, and H. J. Massonne (2004), A counterclockwise PTt path of high-pressure/low-temperature rocks from the Coastal Cordillera accretionary complex of south-central Chile: Constraints for the earliest stage of subduction mass flow, *Lithos*, *75*, 283–310.
Ziegler, P. A. (1987), Late Cretaceous and Cenozoic intra-plate compressional deformations in the Alpine foreland—A geodynamic model, *Tectonophysics*, *137*(1), 389–420.
Ziegler, P. A., S. Cloetingh, and J. D. Van Wees (1995), Dynamics of intra-plate compressional deformation: The Alpine foreland and other examples, *Tectonophysics*, *252*(1), 7–59.